

Home Search Collections Journals About Contact us My IOPscience

# Quadrupole mass spectrometry of reactive plasmas

This article has been downloaded from IOPscience. Please scroll down to see the full text article.

2012 J. Phys. D: Appl. Phys. 45 403001

(http://iopscience.iop.org/0022-3727/45/40/403001)

View the table of contents for this issue, or go to the journal homepage for more

Download details:

IP Address: 134.147.148.109

The article was downloaded on 28/09/2012 at 09:42

Please note that terms and conditions apply.

J. Phys. D: Appl. Phys. 45 (2012) 403001 (23pp)

# TOPICAL REVIEW

# **Quadrupole mass spectrometry of reactive plasmas**

## J Benedikt, A Hecimovic, D Ellerweg and A von Keudell

Research Department Plasmas with Complex Interactions, Ruhr-Universität Bochum, 44780 Bochum, Germany

Received 26 June 2012, in final form 3 August 2012 Published 21 September 2012 Online at stacks.iop.org/JPhysD/45/403001

#### **Abstract**

Reactive plasmas are highly valued for their ability to produce large amounts of reactive radicals and of energetic ions bombarding surrounding surfaces. The non-equilibrium electron driven plasma chemistry is utilized in many applications such as anisotropic etching or deposition of thin films of high-quality materials with unique properties. However, the non-equilibrium character and the high power densities make plasmas very complex and hard to understand. Mass spectrometry (MS) is a very versatile diagnostic method, which has, therefore, a prominent role in the characterization of reactive plasmas. It can access almost all plasma generated species: stable gas-phase products, reactive radicals, positive and negative ions or even internally excited species such as metastables. It can provide absolute densities of neutral particles or energy distribution functions of energetic ions. In particular, plasmas with a rich chemistry, such as hydrocarbon plasmas, could not be understood without MS. This review focuses on quadrupole MS with an electron impact ionization ion source as the most common MS technique applied in plasma analysis. Necessary information for the understanding of this diagnostic and its application and for the proper design and calibration procedure of an MS diagnostic system for quantitative plasma analysis is provided. Important differences between measurements of neutral particles and energetic ions and between the analysis of low pressure and atmospheric pressure plasmas are described and discussed in detail. Moreover, MS-measured ion energy distribution functions in different discharges are discussed and the ability of MS to analyse these distribution functions with time resolution of several microseconds is presented.

(Some figures may appear in colour only in the online journal)

#### 1. Introduction

Low and atmospheric pressure reactive plasmas are a key technology in many industrial applications even dating back more than a century in the cases of ozone generation in a so-called silent discharge [1]. They are irreplaceable in anisotropic etching for microfabrication of printed circuits, they are used to deposit high-added-value layers with optical, electrical, magnetic, mechanical or barrier properties on the surface of a variety of substrates, or they are applied for treatment of living tissue. Plasmas have the advantage of being able to activate any molecular gas by dissociation, excitation or ionization of gas molecules in collisions with

electrons. This property, however, makes plasmas very complex. Energetic electrons, neutral stable species and reactive molecular fragments, positive and negative ions and photons are coexisting and reacting together in one complex mixture. Plasma diagnostics plays, therefore, a crucial role in unravelling the plasma chemistry.

Among many possible diagnostic methods, mass spectrometry (MS) is a diagnostic which offers many advantages for the analysis of reactive plasmas. MS is capable of measuring positive ions, negative ions and neutral species from the plasma including their kinetic energy with time resolutions down to microseconds. MS does not have limitations inherent to optical techniques, such as being

dependent on the existence of suitable optical transitions of the species of interest. MS also measures species in their ground states directly. Once installed on a plasma reactor, MS can provide data for most of the species entering the MS, including low density reactive transient species or even metastables. It should be noted that these advantages also come with several important constraints: the measured species have to be extracted from the plasma reactor into a differentially pumped MS stage and the measurement is, therefore, restricted to the location of the sampling orifice at the wall or at the surface of the electrode. It is also not as sensitive as, for example, some laser based techniques, and it does not provide any information about (ro-)vibrational excitation of the measured species. Quantitative MS measurements are also very sensitive to systematic errors and a very careful design and calibration of the whole measuring system has to be performed.

MS as a microanalytical technique has been experiencing a boom in the last two decades, especially in biological sciences. It has unrivalled sensitivity, provides structural information about analyte and can handle high throughput. The state-of-the-art of MS in microanalytical analysis has been summarized recently by several authors [2–4]. A plasma discharge, however, corresponds to a very peculiar analyte due to the presence of energetic ions, reactive neutral species and photons. The measurement of ion energy distribution functions (IEDFs), densities of short-lived radicals and difficulties connected with the presence of UV and VUV radiation or metastables are usually not covered by the 'standard' MS literature. Additionally, measurements with time resolutions of microseconds are sometimes needed to monitor for example plasma ions in pulsed discharges.

The aim of this review is to focus on these special capabilities of MS with an emphasis on quantitative diagnostics using a quadrupole mass spectrometer (QMS). The review is organized as follows. First, the concise introduction to MS relevant for in situ plasma diagnostics is presented. Second, the issues regarding the connection of the mass spectrometer with the plasma reactor and the proper sampling schemes, especially in the case of detection and analysis of reactive neutral species, are discussed. Afterwards, examples of MS plasma diagnostics for four applications are presented: (i) the measurement of absolutely calibrated and time-resolved densities of stable neutral plasma chemistry products, (ii) the identification and absolute density measurement of short-lived reactive neutral species, (iii) the qualitative measurements of ion fluxes and IEDFs and (iv) the analysis of atmospheric pressure plasmas.

#### 2. Fundamentals of MS

Contemporary MS is a microanalytical technique that is used to detect gas-phase ions generated from a gaseous, liquid or solid sample to determine quantitatively its composition and to reveal the structural information of detected compounds. It is a diagnostic technique with unequalled sensitivity, detection limits, speed and diversity of its applications. It plays a dominant role in biological sciences providing quantitative and structural information at a high throughput. It is also applied

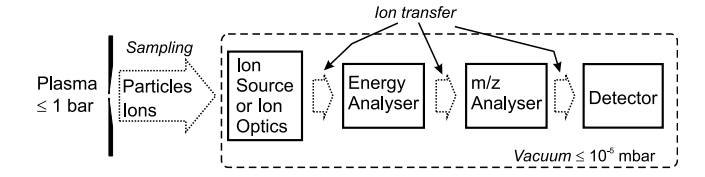


Figure 1. Conceptual illustration of the QMS for plasma analysis.

in fields such as pollution and food control, forensic science, atomic physics, reaction physics and kinetics, inorganic chemical analysis and many others.

Its development started at the end of the 19th century with the discovery of anode rays by E Goldstein (1896) and of the electron and its mass-to-charge ratio being measured by J J Thomson (1897). The first devices capable of measuring mass spectra date back to 1912 and were able to acquire only a few mass spectra per day. Fortunately, mass spectrometers improved in the following decades and they are now an outstanding analytic diagnostic. Many interesting details of the historical development of MS can be found in the literature [3,4]. Nowadays, many powerful mass spectrometers are commercially available offering an unequalled sensitivity, detection limit and speed. They provide full functionality necessary for plasma analysis: measurement of positive and negative ions according to their mass-to-charge ratio (m/z) and energy and measurement of neutrals and their identification with the help of threshold ionization mass spectrometry (TIMS). Current MS instrumentation is well documented in the literature [2–4] and it will, therefore, be only briefly described in this paper with the restriction to the instrumentation most commonly used for plasma analysis. The main issues in MS for plasma diagnostics are the proper design of the particle sampling geometry from the plasma chamber into the MS, the proper relative and absolute calibration of the MS signal including the correction of the background signal, and the correct interpretation of the measured data.

#### 2.1. MS: principle of operation

The principle of MS analysis of plasmas is illustrated in figure 1. Neutral particles or ions originating from the plasma are extracted into the MS at first. Since the measurement is based on the precise manipulation of ion trajectories by electric and magnetic fields, the collisions with other gaseous species have to be avoided. Any mass spectrometer must, therefore, be operated in vacuum with pressures typically below  $10^{-2}$  Pa to assure ion mean free paths much longer than their trajectories in the MS. Even lower operation pressures are required when secondary electron multiplier (SEM) detectors are used. The mass spectrometer must, therefore, be placed inside a differentially pumped vacuum chamber and the measured neutrals or ions have to be extracted through a sampling orifice or narrow tubing. This extraction is critical for the quantitative interpretation of the measured data and will be discussed separately in the next section.

The analysis of the sampled particles is different for neutrals and ions. In the case of neutrals, ionization has to take place first to generate charged species. In the case of ions,

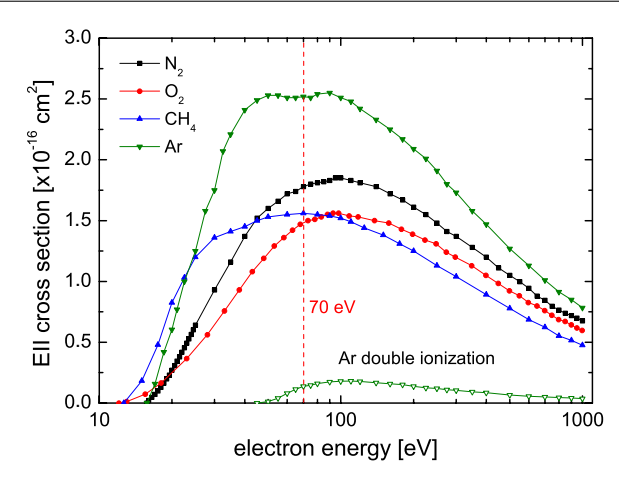


**Figure 2.** Electron impact ionization cross-section for different gases as a function of the electron energy. Data taken from [6, 7].

ion extraction optics is used to focus the sampled ions into the mass spectrometer. All ions are then transferred through the energy analyser (usually optional for the measurement of neutral particles) and m/z analyser to finally reach the detector, where an electrical signal as a current or TTL pulses is generated. The electron impact ionization process and the MS instrumentation, namely the ion transfer optics, ionizers, energy filters, quadrupole mass filter and detectors used in the MS for plasma analysis will be discussed in the following.

2.1.1. Electron impact ionization. Electron impact ionization (EII) can be described as a collision between a free incoming electron and a valence electron of a target atom or molecule, in which sufficient energy is transferred to the valence electron for its ionization. The direct EII collision without fragmentation of the molecule and without multiple ionization can be expressed as

$$M + e^- \rightarrow M^+ + 2 e^-.$$
 (1)

The dependence of the EII cross-section on the energy of the incoming electron can be described reasonably well by the Thomson formula derived from a classical treatment of this collision under the assumption of small angle scattering [5]. Quantum mechanical treatment is necessary for the rigorous calculation of this collision. The EII cross-section is zero below a threshold energy, which is the ionization energy of the valence electron of a given species, and rises linearly just above this energy. The cross-section reaches its maximum at energies around  $50-100\,\mathrm{eV}$ , followed by a slow decrease at higher energies. EII is a non-resonant process in which the free electrons can carry excess kinetic energy. Examples of cross-sections for the direct EII process for  $N_2$ ,  $O_2$ ,  $CH_4$  and Ar are shown in figure 2.

EII can also result in multiple ionization of the target particle (MEII, reaction (2)), dissociative ionization of a target molecule (DEII, reaction (3)) or even in the formation of multiply charged molecular ion fragments:

$$M + e^- \rightarrow M^{z+} + (z+1)e^-,$$
 (2)

$$ABC + e^{-} \rightarrow AB^{+} + C + 2e^{-},$$
 (3)

$$\rightarrow AC^+ + B + 2e^-, \tag{4}$$

$$AB + e^- \to A^- + B. \tag{5}$$

In the case of MEII, one needs to take into account that the  $M^{z+}$  ions appear in the mass spectrum at a mass divided by the number of elementary charges z.

The dissociative electron impact ionization (DEII) proceeds through the formation of the molecular ion in its repulsive non-bonding state, which dissociates quickly in one ionized and one or several neutral fragments. The atoms in the fragments rearrange in comparison with the original molecule (reaction (4)). The statistical distribution of different dissociative ionization channels, the cracking pattern (CP) or fragmentation pattern, is an intrinsic property of the given molecule (in its ground state and at standard temperature) and depends only on the electron kinetic energy. It is described by electron energy-dependent dissociative ionization crosssections. An example of the DEII cross-sections for the CH<sub>4</sub> molecule and its CP, as measured at an electron energy of 70 eV, are shown in figure 3. The most intense peak in the CP is the molecular ion  $CH_4^+$  at m/z = 16, followed by the  $CH_3^+$  ion at m/z = 15. The probability that more than one H atom are lost in the DEII is very low with correspondingly small crosssections. The CP has additionally a peak at m/z = 17, which is caused by the presence of C and H isotopes (mainly <sup>13</sup>C). A given molecule can be identified based on the measurement of its CP. The measured mass spectra are, however, influenced by mass and energy-dependent transmission functions of the given mass spectrometer, which needs to be considered or calibrated (see below).

Molecular ions are often unstable after EII and, therefore, ionization is always dissociative. For example, the hexamethyldisiloxane molecule (HMDSO) looses one methyl group after ionization and the heaviest ion fragment is measured at m/z = 147 and not at 162 [8].

Threshold energies of MEII and DEII are higher than that of direct EII, because either some additional electrons have to be removed from the valence state or at least one chemical bond has to be broken, respectively. This energy difference is very important for identification and quantification of molecular fragments directly originating from the plasma by TIMS. On the other hand, the thresholds for MEII and DEII are lower than the energy, at which direct EII cross-sections reach their maxima and where the mass spectra are typically recorded ( $E_{\rm el} = 70 \, {\rm eV}$ , see the cross-section for MEII of Ar in figures 2 and 3 for DEII of CH<sub>4</sub>).

Cross-sections for EII processes can be measured with high accuracy in electron-molecule cross beam experiments [10]. They are available for many stable molecules (see for example the compilation of the literature data in Landolt-Börnstein [6] for  $H_2$ ,  $H_2O$ ,  $CH_3Br$ ,  $CH_3Cl$ ,  $CH_3F$ ,  $CH_3I$ ,  $CH_4$ ,  $Br_2$ ,  $Cl_2$ ,  $F_2$ ,  $NF_3$ ,  $SiF_4$ ,  $SF_6$ ,  $CCl_2F_2$ ,  $CCl_4$ ,  $CF_4$ ,  $CH_3OH$ , CO, COS,  $CO_2$ , CS,  $CS_2$ ,  $C_2F_6$ ,  $CH_4$ ,  $C_2H_2$ ,  $C_2H_4$ ,  $C_2H_6$ ,  $C_3F_8$ ,  $C_{60}$ ,  $UF_6$ ,  $H_2S$ ,  $NH_3$ ,  $SiH_4$ ,  $Si_2H_6$ , NO,  $NO_2$ ,  $N_2$ ,  $N_2O$ ,  $O_2$ ,  $O_3$ ,  $SO_2$ ,  $S_2$ ), atoms [7, 11] and even molecular fragments such as  $CD_x$  (x = 1-4) [12, 13] or  $SiH_x$  (x = 1-3) [14]. The unknown EII cross-sections of molecular fragments can also be calculated, with very good agreement with experimental data,

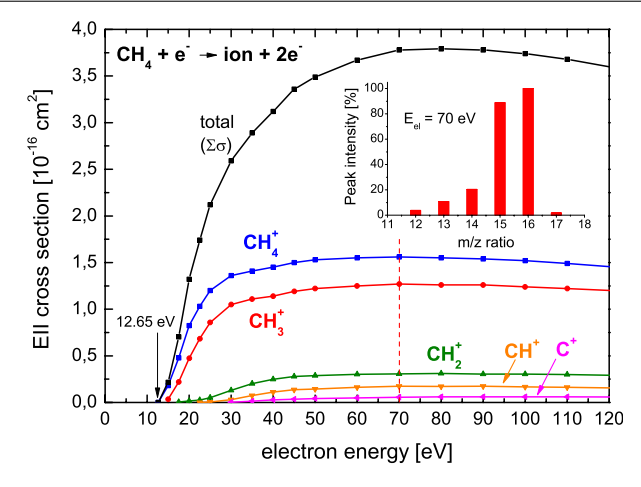


**Figure 3.** The direct and dissociative EII cross-sections for  $CH_4$  molecule [6] and its CP at  $E_{el} = 70 \, eV$  [9].

see for example the data for  $SiH_x$  (x = 1-3) and  $GeH_x$  (x = 1-3) [15]. Additionally, the unknown EII cross-sections can also be estimated. In the case of hydrocarbon molecules, the cross-sections have very similar slopes in the near-threshold energy region and have typical maximum values of a few  $10^{-16}$  cm<sup>2</sup>. The total EII cross-section scales approximately with the size of the hydrocarbon molecule in the electron energy range above  $20 \, \text{eV}$ , following empirical additivity rules [16].

The collision of an electronegative molecule with an electron can also result in electron capture and the formation of a negative ion in the so-called dissociative electron attachment (DEA) reaction (5). This process is a resonant process, because the incoming electron is captured and cannot carry away the excess kinetic energy. It proceeds through the formation of a short-lived negative-ion resonance (NIR), in which the incoming electron is captured into a low-lying unoccupied molecular orbital having typically anti-bonding character. The geometry of the NIR complex (interatomic distances and bond angles) starts to rearrange in response to the new electronic structure and a repulsive force may be develop when the NIR is formed. When the lifetime of the NIR is long enough, dissociative attachment results in the formation of a stable negative-ion fragment of the original particle [17, 18]. The resonant character of DEA explains also the characteristic shape of the energy dependence of the cross-sections with their bell-shaped maxima at resonant energies. The position of these maxima can be used for the identification of given molecule.

Alternative ionization methods to EII are for example photoionization or chemical ionization [4]. The most popular example of the latter one is the proton transfer ionization [19]. The discussion of these ionization methods is out of the scope of this paper.

#### 2.2. Concise introduction to mass spectrometer components

2.2.1. Ion optics. As already mentioned, ions can be directly measured by focusing them with electrostatic lenses into the MS. The mass spectrometers for plasma analysis are equipped with lenses installed in front of the ionizer and detection of both plasma generated ions or neutrals is possible with the very same device. An example of the principle of operation of an ion

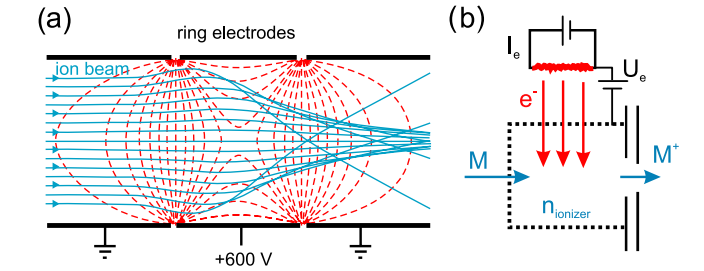


**Figure 4.** Schematic sketch of ion beam focusing in an electrostatic ion lens (after Simion simulation SW [23]) (*a*) and schematic representation of electron impact ionizer (*b*).

lens is shown in figure 4(a). As will be discussed later, Hamers  $et\,al\,[20]$  have shown that the focal length of the lens can change with ion energy leading to a chromatic abberation, which has to be taken into account for quantitative measurements. Various configurations of ion lenses (RF-only driven quadrupoles, hexapoles or octupoles) are used to transfer ions between different components of mass spectrometer [3].

2.2.2. *Ionizers*. A variety of different ionization methods are known such as EII, DEA, chemical ionization, thermal ionization or photoionization. The vast majority of MS studies of low temperature plasmas involve EII and we will restrict ourselves to this ionization method.

Most important in EII is the generation of electrons with a well defined and narrow energy distribution function in the region where the electrons interact with the sampled gaseous particles. The schematic view of the principle of operation of electron impact ionizer is shown in figure 4(b).

The electrons are generated by thermionic emission from a current-heated filament. The material of the filament can be tungsten for not-oxidizing gas mixtures and thorinated iridium for gas mixtures with oxygen. The electrons are accelerated towards the ionizer by a potential difference between the filament and the ionizer cage. The electrons are monoenergetic with an energy spread of  $\Delta E_{\rm elect} \sim 0.5 \, {\rm eV}$  caused mainly by the voltage drop across the filament. This energy spread can be further reduced using a cross-beam electron ionizer.

The electron emission rate is measured as an electron current between filament and the ionizer cage (emission current) and is controlled by the filament temperature (heating current). The ionization rate in the ionizer is proportional to the emission current up to the point where space charge effects start to play a role and the proportionality is not guaranteed any more [21]. It should be noted that the presence of hot filaments in the ionizer can lead to the generation of additional species at their hot surface (for example, the H<sub>2</sub>O, CO or CH<sub>4</sub> are generated in the presence of  $H_2$  gas [22]), which complicates the analysis of the measured mass spectra. This is, for example, especially important for detecting atomic hydrogen from plasmas: H<sub>2</sub> entering the MS is usually poorly pumped and, therefore, a background pressure will build up in the MS. This background H<sub>2</sub> dissociates at the hot filament, leading to a partial pressure of H inside the MS. This internal generation of H may be larger than the sampled H from the plasma, making the detection of plasma generated H impossible.

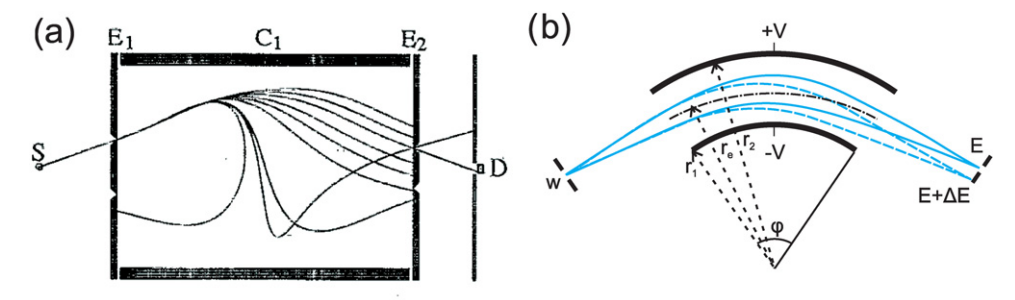


**Figure 5.** Ion trajectories within (a) the Bessel box (reprinted with permission from [28], copyright 1995, American Institute of Physics) and (b) schematic representation of electrostatic energy analyser (ESA).

2.2.3. Energy analysis. The selection of ions with respect to their energy is performed using energy analysers with several designs, out of which two are widespread, namely Bessel box type energy analysers and sector field electrostatic energy analysers. A third design, rarely used, is the Wien filter [24]. The Bessel box energy analyser (BBEA) was first reported by Allen et al [25] as an alternative to existing energy analysers with the advantage of its simple design. The concept is to create a bandpass ion energy filter with a resolution of 0.5 eV. The BBEA is a cylindrical vessel with end caps insulated from the body of the analyser. Each end cap has a circular aperture in the centre. In the centre of the cylinder an obstruction is placed with the aim to block line-of-sight transmission of highenergy particles (see figure 5(a)). By applying a potential to the cylinder, a potential barrier is created for low-energy particles disabling them to exit through the second end cap. A field created by the potential applied between cylinder and end caps bends the trajectory of ions with higher energy. As a result, ions with chosen energy will exit through the second end cap [26–28]. The trajectories of the ions within the BBEA can be described with modified Bessel functions, giving the name of the device. Sweeping the voltage on the cylinder and end caps while keeping the potential difference constant, IEDF can be measured. The advantage of the Bessel box is its simple design and minimal field perturbation near the slits yielding energy resolutions below 0.5 eV [28]. The disadvantage is the shape of the field, which does not allow a simple description of the focusing and dispersion properties. Finally, the transmission efficiency of BBEA is only around 10%.

Other commonly used energy analysers are sector field electrostatic energy analysers (ESAs). The concept is to use an electrostatic field produced between two charged electrodes. The electrodes may exhibit several configurations; parallel plate, cylindrical, spherical or toroidal configurations [29]. Very frequent ESAs are cylindrical analysers with a sector angle of  $45^{\circ}$  or  $90^{\circ}$  (figure 5(b)). The electric field  $E_0 = V_0/d$ , where d is the plate distance, is chosen to guide ions entering the ESA with an energy  $E_{\rm ion}$  on a circular trajectory along the optical axis. The centripetal force generated by the electric field has to balance the centrifugal force:

$$zeE_0 = \frac{mv_0^2}{r_e} = \frac{2E_{\text{ion}}}{r_e} \to E_0 = \frac{2E_{\text{ion}}}{zer_e},$$
 (6)

where z is the charge state of the ion. For ions with trajectories on the optical axis  $r_e$  the following relations between the energy

of the particle E and applied voltage is valid for cylindrical electrodes [30].

$$E_{\rm ion} = \frac{ZeV_0}{2\ln(r_2/r_1)}. (7)$$

Ions entering the ESA are deflected according to their kinetic energy and independent of their m/z ratio. The energy resolution of the ESA is given by equation:

$$\Delta E_{\rm ion} = \frac{w E_{\rm ion}}{r_{\rm e}(1 - \cos \varphi) + L \sin \varphi},\tag{8}$$

where w is the aperture width,  $\varphi$  is the sector angle and L is the distance through the sector. The advantage of the sector field is its 100% transmission for ions with the selected energy. However, since the ion trajectories are bent by 45°, an ESA is much more space demanding.

2.2.4. Mass analysis. Ions leaving the ion source are deflected by an extraction electrode into the mass analyser. The mass analyser is responsible for the ion separation based on their m/z ratio. Generally, one categorizes a mass spectrometer by the type of mass analyser. There are several different types of mass analysers known, such as TOF, electric or magnetic sector field, linear quadrupole or ion trap [3]. Despite their different ion-separation techniques, all of them have in common that they use static and/or dynamic electric and/or magnetic fields for ion-separation. As already announced, we will discuss just the transmission quadrupole (TQP) mass filter, invented by Paul and Steinwendel in 1953 [31], as the most commonly used mass analyser in the MS of plasmas. Quadrupole MS (QMS) is usually chosen due to its low cost, light weight, compact design, simple operation and high scan speed. In contrast, the TQP has relatively low resolution ( $\sim 0.3 \, m/z$ ) and the transmission function is mass dependent with a discrimination of heavy ions [3]. It is also inherently difficult to measure quantitatively very light atoms such as atomic hydrogen.

Figure 6 presents the schematics of the quadrupole filter. Four parallel rods are biased by dc and RF voltages with the opposite rods being at the same potential. A time dependent quadrupole field is generated in this way. Ions entering the TQP move on trajectories modulated in the x- and y-directions by the changing quadrupole field. The dc and RF components of the field can now be selected in such a way that only ions with selected m/z ratio have stable trajectories with limited

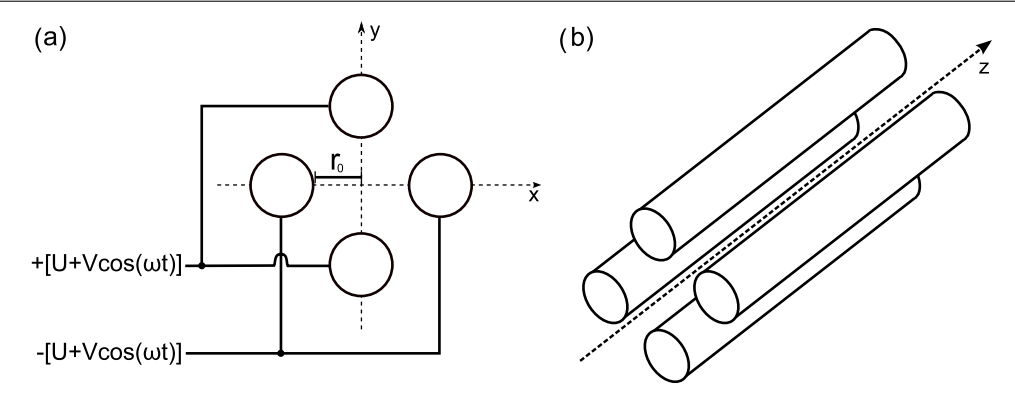
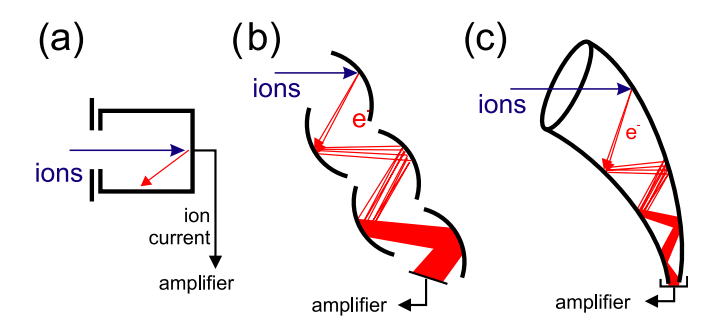


Figure 6. Cross-section, electrical connection (a), and schematic (b) of a cylindrical quadrupole mass analyser.



**Figure 7.** Ion detectors: (*a*) Faraday cup, (*b*) SEM with discrete dynodes and (*c*) SEM with one continuous dynode.

oscillations around the z-axis. All other ions are deflected from the axis and are lost on the rods, because the amplitude of their oscillations is either in the x- or in y-direction unstable. The mathematical treatment of TQP with the solution of Mathieu equation and with the discussion of the stability diagram has been published many times and will not be repeated here [2, 4].

2.2.5. Ion detection. After the ions have been separated based on their m/z ratio, they need to be transformed into a measurable signal. This is carried out by an ion detector. The simplest detector for ions is a Faraday cup, figure 7(a). The Faraday cup consists of a metal cup that collects all ions leaving the mass filter. It has a cup-like shape to recapture secondary electrons that are created upon ion impact. The current flowing away from the Faraday cup is transformed by a resistor of high-impedance into a voltage. This voltage is proportional to the collected ion current constituting the signal for further analysis. The sensitivity of a Faraday cup does not deteriorate with time and does not dependent on the ion mass like a SEM. However, the sensitivity is relatively low and the response time is slow.

The most common detector used in MS is a SEM, which can be built with discrete dynodes, figure 7(b), or with one continuous dynode, figure 7(c). An SEM with discrete dynodes contains a conversion dynode at a high potential whose polarity is opposed to the charge of the ions leaving the mass filter. The ions are hence accelerated towards this conversion dynode and impinge on it. This causes emission of several secondary electrons which are again accelerated towards the following dynode. The following

electron multiplier consisting of several dynodes amplifies the secondary electron current in a cascade process with a gain of around 10<sup>5</sup> or more. The amplified electron current is collected by an electrode and then converted into a voltage signal that is proportional to the number of impinging ions. The principle is similar for a SEM with continuous dynode, where the electrons are multiplied during several consecutive impacts on one dynode made of a material with high resistance and therefore a high voltage drop along its length.

The advantage of an SEM in contrast to a Faraday cup is the high amplification factor and the fast response time. However, the lifetime of an SEM is limited and the operating voltage has to be adjusted regularly. The impact of ions on the dynodes leads to a contamination of their surface and hence to a decreasing amplification. Furthermore, the gain of SEMs depends on the ion velocity. Because ions are impinging on the first dynode with constant energy the SEM generates lower signal for heavier ions.

General remark. The sensitivity of quadrupole mass spectrometers changes in time due to (i) the change in the efficiency of the ionizer (filament conditions) and (ii) drifts in the sensitivity of the SEM ion detectors [32]. Therefore, any absolute calibration of measured signals should be performed repeatedly (weekly basis) and after any significant change in the measuring system such as pressurization or exchange of filaments or detector.

# 3. Sampling strategies of stable, reactive and charged species from the plasma reactor

The design of the gas sampling system, namely the differentially pumped multiple stages is crucial for the successful detection of highly reactive low density particles and for correct determination of their densities. Additionally, the most proper sampling scheme is different for the measurement of neutral species (stable or reactive) and of ions. The necessary considerations in the design of the MS sampling and measuring systems will, therefore, be discussed in detail in this section.

#### 3.1. Sampling of neutral species

One of the most powerful features of plasma MS is the ability to measure absolute densities of neutral species including highly

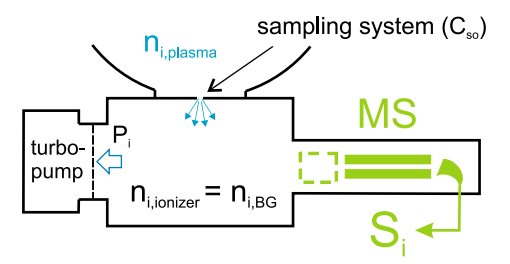


Figure 8. Schematics of the single stage RGA.

reactive radicals. These neutral species have to be ionized in the ionizer prior to their analysis and detection. The measured signal  $S_i$  of species i, as recorded by a given mass spectrometer, is linearly proportional to the density of species i in its ionizer  $n_{i,\text{ionizer}}$  and is given by [33]

$$S_i = n_{i,\text{ionizer}} \sigma_i(E_{el}) \beta l_{\text{ionizer}} I_e T(m_i) \theta(m_i), \tag{9}$$

where  $\sigma_i(E_{\rm el})$  is the electron energy-dependent EII cross-section for the formation of the given (fragment) ion,  $\beta$  is the ion extraction efficiency of the ionizer,  $l_{\rm ionizer}$  is the length of the ionizer,  $I_{\rm e}$  is the electron emission current in the ionizer,  $T(m_i)$  is the mass-to-charge ratio dependent transmission function of the quadrupole and ion transfer optics and  $\theta(m_i)$  is the mass-to-charge ratio dependent sensitivity of the detector. This signal needs to be calibrated to obtain absolute densities. This calibration, described in the following, depends on the properties of the particles of interest.

3.1.1. Sampling of stable neutral species. The measurement of densities of stable species is the most easiest and also the most common task of plasma MS. It can be achieved by low cost devices (also called residual gas analysers, RGA) with fixed electron energy (typically 70 eV) and with a single differentially pumped vacuum stage housing the mass spectrometer. The schematic representation of the measurement is shown in figure 8.

The density of the measured species in the ionizer  $n_{i,\text{ionizer}}$  is equal to its background density in the differential pumping stage  $n_{i,\text{BG}}$  and is determined by the equilibrium between particle inflow through the sampling orifice  $F_{i,\text{so}}(s^{-1})$  and the pumping speed of the given turbomolecular pump  $P_i$  m<sup>3</sup> (s<sup>-1</sup>). The sampling orifice can be replaced by a leak valve or a long narrow tube. The background density  $n_{i,\text{BG}}$  can be expressed as

$$n_{i,\text{ionizer}} = n_{i,\text{BG}} = \frac{F_{i,\text{so}}}{P_i} = \frac{n_{i,\text{plasma}}C_{\text{so}}}{P_i},$$
 (10)

where  $C_{\rm so}$  is the conductivity of the sampling orifice, leak valve or connection tube. This conductivity is  $C_{\rm so}=0.25v_iA_{\rm so}$  for an infinitely thin orifice with an area  $A_{\rm so}$  under molecular flow conditions (diameter  $d_{\rm so}\ll\lambda_{\rm mfp}$ , particle mean free path in the reactor). The velocity  $v_i$  is the mean velocity given by  $(8k_{\rm B}T_i/\pi/m_i)^{0.5}$ . Equation (10) shows that the density in the ionizer is linearly proportional to the density in the plasma reactor and square root dependent on  $T_i$ . The square root dependence on  $m_i$  in the expression for  $v_i$  cancels with the same dependence of the pumping speed, which is also scaling with particle velocity.

Since the gas for RGA is usually sampled at the reactor wall far from the 'hot' plasma region, the gas temperature dependence can be neglected in most cases. The relative changes of the measured signal for a given species are, therefore, proportional to the variation of its density in the reactor. The absolute calibration of the signal is very easy for stable gases available in bottles, because the scaling factor between the density in the reactor and the measured signal can be determined by an additional calibration measurement of the gas at known density in the reactor. This measurement also provides directly the CP for the given molecule, provided the BG signal and the signal due to possible impurities in the gas bottle or gas lines have been subtracted.

The density calibration of molecules, which are not available from an external supply (for example unstable unsaturated hydrocarbon molecules often generated in hydrocarbon plasmas) can be estimated based on the comparison between two measurements: (i) a calibration measurement of an available gas A (calibration gas) at a known density in the reactor; (ii) the measurement of the species of interest B in the reactor. If the EII cross-sections of A and B are known as well as the mass-dependent transmission efficiency of the mass spectrometer, the density of species B can be extracted from that comparison. An example of such a calibration campaign of stable species with known EII cross-section and CP, but also the possible method of estimation of unknown fragmentation patterns and densities of plasma generated molecules, is given in the next section of this paper.

3.1.2. Sampling of reactive transient neutral species. detection and proper density calibration of reactive neutral species is much more demanding. They are lost in collisions with the walls of the vacuum chamber and with the mass spectrometer itself and their background density in the mass spectrometer chamber decreases. Consequently, with increasing distance from the sampling orifice to the ionizer in the MS, the reactive species density is much smaller than the background density of stable species. Additionally, the background density strongly depends on the surface reaction probability, which is very often unknown. The molecular beam (MB) sampling scheme, where wall collisions of the sampled species are avoided, must therefore be used. This sampling technique uses several pumping stages, which are connected by small orifices aligned on one axis between the sampling orifice and the ionizer.

A schematic representation of a system using two pumping stages is shown in figure 9. The gas mixture is sampled from the plasma reactor through the sampling orifice with area  $A_1$  into the 1st pumping stage. It is important that the sampling orifice has in this case a very low aspect ratio to avoid particle collisions within the orifice side walls to ensure that the sampled beam has the same cosine distribution for all sampled particles. Most of the sampled particles are pumped away by the turbomolecular pump in the 1st stage, only a narrow solid angle of the particles transits directly into the 2nd pumping stage through the 2nd orifice with area  $A_2$ , where a slightly divergent MB is formed. This beam is then passing the ionizer of the mass spectrometer and provides hence a direct

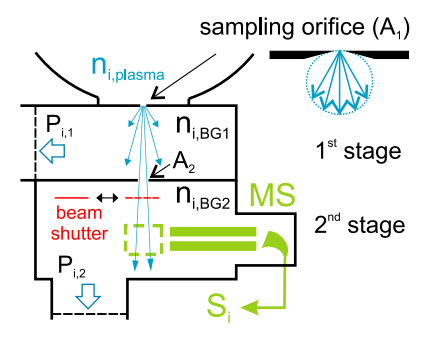


**Figure 9.** Schematics of the sampling system with two differentially pumped stages.

connection of the plasma to the ionizer. Moreover, the number density in the MB at distance x from the sampling orifice with radius  $r_1(x \gg r_1)$  is independent of the mass or temperature and is given as [34]

$$n_{i,\text{beam}} = \frac{1}{4} n_{i,\text{plasma}} \left(\frac{r_1}{x}\right)^2. \tag{11}$$

This expression is valid under molecular flow conditions.

The signal is, however, still determined by the total species density in the ionizer, which is now given by the sum of the beam density and the background density in the 2nd stage. Therefore, a beam chopper has to be used in the 2nd stage. The signal due to the MB particles is then determined as the difference between the signals measured without and with chopper blocking the MB. This beam signal  $S_{\text{beam}}$  is given by

$$S_{i,\text{beam}} = \frac{1}{4} n_{i,\text{plasma}} \left(\frac{r_i}{x}\right)^2 \sigma_i(E_{\text{el}}) \beta l_{\text{ionizer}} I_{\text{e}} T(m_i) \theta(m_i). \quad (12)$$

The unknown density of some reactive particle i can be determined by comparing its measured beam signal  $S_{i,\text{beam}}$  with the beam signal for some stable calibration species with known density  $S_{\text{cal},\text{beam}}$ . Dividing expressions (12) for both species and rearranging, the unknown number density can be expressed as

$$n_{i,\text{plasma}} = F(m_i, m_{\text{cal}}) \cdot \frac{n_{\text{cal,beam}} \sigma_{\text{cal}}(E_{\text{el}})}{S_{\text{cal,beam}} \sigma_i(E_{\text{el}})} S_{i,\text{plasma}}$$
(13)

with the mass-dependent transmission function  $F(m_i, m_{\rm cal}) = T(m_{\rm cal})\theta(m_{\rm cal})/(T(m_i)\theta(m_i))$ . Since  $F(m_i, m_{\rm cal})$  is a function of the mass-to-charge ratio only, F is equal to unity when species i and calibration species cal have the same mass. Otherwise, F can be determined by measuring different gases with known EII cross-sections and known densities in the ionizer [35]. For such a comparison, it is crucial to select only ions that are created via direct EII and not via DEII, because the high kinetic energy of the fragment ion in DEII, can result in very low extraction efficiencies from the ionizer [36].

An excellent example of the MS measurements of absolute densities of  $CF_x$  radicals from the  $CF_4$  plasma was reported by Singh *et al* [33]. In this work, the performance of the MS sampling system with only one or with three differentially pumped stages is compared. It demonstrates very clearly the advantages of a sampling system with several pumping stages and it will therefore be discussed here in more detail.

**Table 1.** Comparison of experimental parameters for single and triple pumping stage system as reported by Singh *et al* [33].

Parameter	Single stage	Triple stage
Sampling orifice diameter (µm)	150	900
Sampling orifice-ionizer distance (mm)	135	353
$n_{i,\text{beam,ionizer}}/n_{i,\text{plasma}}$ ratio	$0.3 \times 10^{-6}$	$1.6 \times 10^{-6}$
Effective pumping speed in the last stage (l min <sup>-1</sup> )	~142	~212

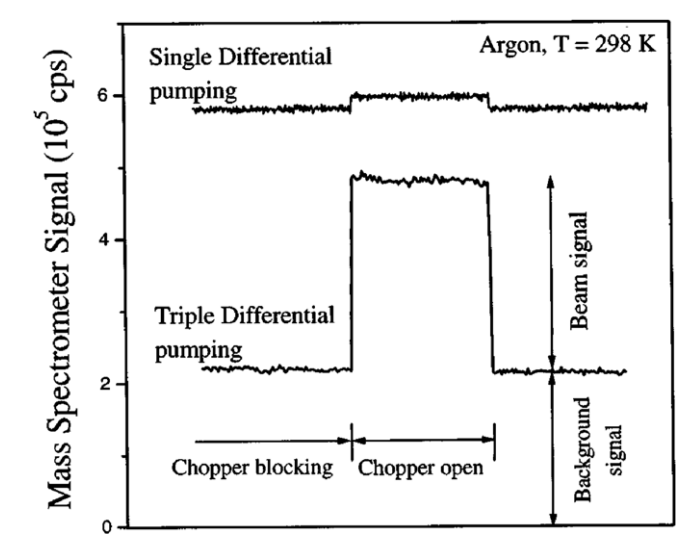


**Figure 10.** Comparison of the beam-to-background ratio for argon gas measured sampling system with single and triple differential pumping. Reprinted with permission from [33], copyright 1999, American Vacuum Society.

The parameters of the single and triple differential pumping systems in this example are summarized in table 1 and the measured signals with chopper open and chopper blocking the MB for both systems are shown in figure 10. The diameter of the sampling orifice has to be very small for the single stage system to maintain the low pressure in the mass spectrometer. The sampling orifice can be much larger in the triple stage, because the multiple pumping stages can easily maintain a low pressure in the last stage housing the mass spectrometer. The area of the sampling orifice for the triple stage is 36 times larger than for the single stage overcompensating, thereby, the longer distance between the sampling orifice and the ionizer in the triple system. The calculated beam density in the ionizer is more than 5 times larger for the triple stage. The difference of the measured beam density between the single and triple stage systems in figure 10 is even larger, although one may assume that the measurements have not been performed at the same time and the sensitivity of the MS was therefore very probably different for both curves. Moreover, and it is as important as the beam signal intensity, the beam-to-background ratio is improved from 0.029 for the single stage to 1.20 for the triple stage. An additional advantage of the larger sampling orifice is the fact that it is not so easily clogged or influenced by the deposition of thin films, prolonging, therefore, the time between orifice replacement or cleaning.

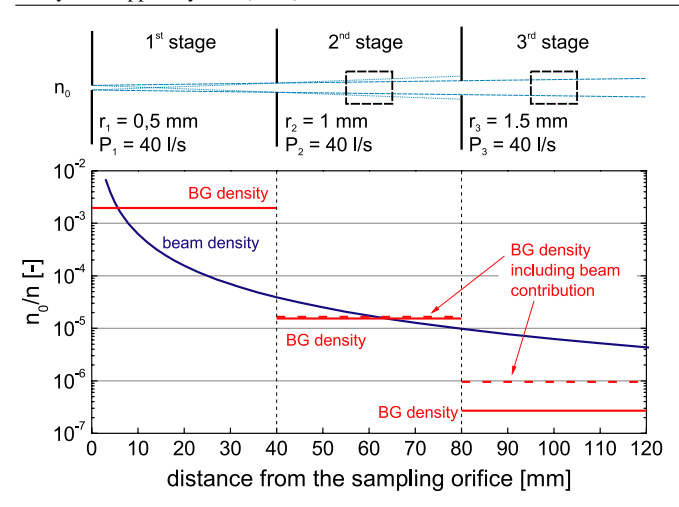


**Figure 11.** Model calculation of beam and BG densities in the differentially pumped stages of the sampling system. The BG density is calculated for two cases: (i) solid red line: the beam particles are not taken into account as a source of BG density and (ii) dashed red line: the beam particle are added as a source of BG particles.

The advantage of the multiple stage system and the difference between systems with two and three stages is illustrated in figure 11. The blue line represents the model calculation of the beam density (equation (11)) and the red solid lines the BG densities in the three pumping stages. The background pressure in the 1st pumping stage is given by the formula (10), because the particle loss through the second orifice is negligible. The same formula can be used to estimate the background densities in the following vacuum stages, when the background density of the previous stage and the conductivity of the connecting orifice are used in equation (10) for more detailed description and model calculation (see [33, 35]). The sampling orifice with a radius of 0.5 mm and the additional orifices with radii of 1.0 mm, and 1.5 mm, respectively, are used. All stages are for simplicity pumped by 40 l/s pumps (realistic estimation of an effective pumping speed at a 63 mm diameter CF flange).

The beam density drops rapidly with distance below the BG density in the 1st stage. Both are proportional to the area of the sampling orifice and therefore their ratio does not change when the size of the sampling orifice is changed. The BG density can be selectively reduced by increasing dramatically the pumping speed, which is, however, not possible due to geometrical limitations. The BG density in the 2nd stage is roughly 100 times smaller compared with the first stage and is now comparable to the beam density. An addition of the 3rd stage reduces the BG density even further ( $\sim$ 50 times, solid red line). However, the beam itself is now a source of BG particles and contributes significantly to the BG density. Note that the beam density at the 3rd orifice ( $x = 80 \,\mathrm{mm}$ ) is almost as high as the BG density in the second stage. Additionally, all beam particles move in the direction to the 3rd stage whereas only 1/4 of BG particles enter on average the 3rd hole. Therefore, the beam particles are the most dominant source of BG in the 3rd stage. The BG density increases  $\sim$ 3.5 times when the beam particles are considered as the source of BG (indicated as a dashed red line in figure 11). This can be a problem, when the beam chopper is placed in the 2nd stage and not in the 3rd stage, because the BG density changes as the beam is blocked. Not considering this effect will result in a measurement of unnaturally high beam-to-background ratios and lead to a systematic underestimation of densities of reactive species in the calibration process, because their BG component of the MS signal is much smaller or even negligible. We have observed for a triple stage system that 84% of the BG signal originates from the beam particles [35].

The effect of the additional BG density due to the beam particles can be also observed in a system with only two pumping stages. However, because the beam density at the 2nd orifice (x = 40 mm) is much smaller than the BG density in the first stage, the beam particles account in our model calculation only for about 5% of the BG density (the beam part of the BG will, however, increase, when the 2nd sampling orifice is placed closer to the sampling orifice). MS sampling systems with two stages and a beam chopper in the 1st stage have been, for example, reported by [37, 38] and the BG signal in the 2nd stage due to the beam particles was about 6% of the total BG signal. The problem with the changing BG density in the MS stage, if the chopper is placed in the previous stage, can be overcome using a chopping period, which is shorter than the particle residence time in the MS stage [35].

It should be mentioned that the beam density shown in figure 11 does not correspond directly to the measured beam component of the MS signal. The beam density is independent of the radii of the 2nd and 3rd orifice, but the beam diameter, and with that also the absolute number of beam particles in the ionizer, will change because the beam is not filling the whole ionizer, in contrast to the BG density (an ionizer with 7 mm diameter is indicated in figure 11 as well to illustrate this effect). Our model calculation represents, therefore, the best scenario for optimum beam signal components and the measured beam component of the signal may be even smaller in reality.

The model calculation shows that systems with just two pumping stages should be satisfactory in most cases for the analysis of low-pressure plasmas in comparison with triple stage systems. The double stage pumping system is simple in design and the ionizer can be placed in general more closer to the sampling orifice, where the beam density is larger, and the BG density is suppressed to the level comparable to the beam density. Adding the third stage does not provide such an advantage in the beam-to-background ratio as is the case by adding the second stage, because the beam particles contribute significantly to the BG density in the third stage. A triple pumping stage system should only be used, when the BG density is really a concern for the measured signal or when higher pressure plasmas are analysed and the three stages are necessary to achieve the desired pressure. For example, beamto-background ratios of about one [33, 35] have been reported for triple differential pumping systems, but only a slightly worse ratio of 0.3 has been reported for a double system [37].

An additional problem can arise from the geometry of the ionizer itself. An ionizer in a closed metal housing is quite often used with only two opening holes, one for the entrance of the beam and the other for the extraction of ions. The stable particles in the MB, which enter the ionizer and collide with one of its parts, cannot easily leave it and build up a significant background density, which can be several times higher than the beam density causing a systematic error in density calibration of reactive particles. It was shown recently, with a simple Monte Carlo simulation of particle trajectories inside the ionizer, that this effect can explain the experimentally observed discrepancy of a factor of three between growth fluxes, calculated from measured and calibrated densities of reactive species, and overall film growth rate [39].

#### 3.2. Sampling of positive and negative ions

The detection of plasma generated ions differs from neutral particle detection. At first, in the case of neutral species densities are measured, whereas in the case of ions fluxes are measured. These fluxes are larger for lighter ions due to their higher velocity at the same ion density and ion energy. Second, there is no ion background density in the mass spectrometer and therefore no beam chopper or background subtraction is necessary. Only single differential pumping stages are therefore required. However, the difficulty in ion MS arises from the fact that ions must be extracted directly via the ion extraction optics of the mass spectrometer, which has to be in line of sight with the sampling orifice.

The extractor electrode is the first electrode in the set of ion optics electrodes. By detecting positive ions, a negative bias on this extractor electrode is applied having a dual role. It attracts positive ions of interest and repels electrons and negative ions (negative ions can be detected by reversing the polarity of all electrodes). Extensive studies of the influence of the potentials applied to the ion optics electrodes on the ion trajectory have been carried out by Hamers *et al* [20]. They have shown a large significance of applying the appropriate potential on the ion optics electrodes in order to avoid chromatic aberration, i.e. the change in the focal length with ion energy, which would result in an alteration of the shape of the ion beam entering the energy analyser with ion energy.

Several authors reported the dependence of the acceptance angle of the mass spectrometer on the ion energy [20, 40, 41]. The acceptance angle is reported to be an exponential decay function of the ion energy with values between 5° and 23° for ions with energy below 1 eV, and for ions with energy higher than 1 eV the angle value is approximately 3° degrees depending on the model of the mass spectrometer. Furthermore, Hamers *et al* reported that the acceptance angle function depends on the potential applied to the extractor electrode, with less steeper function of the angle for lower absolute values of the potential.

The sheath potential formed in front of the MS orifice accelerates positive ions towards the orifice; however, it repels negative ions with kinetic energy lower than the sheath potential. One solution for measuring negative ions is to isolate the orifice and to apply a positive bias to bend the local sheath potential. However, this positive bias would generate large electron currents possibly creating even more negative ions [42]. Another solution is to measure negative ions in

the off phase of the pulsed discharge [43–46]. It is of great importance that the off-time is sufficiently long to allow the diffusion of negative ions to the wall and to the sampling orifice.

# 4. Measurement and quantification of neutral species

#### 4.1. Measurement of stable neutral species

The densities of precursor gases and stable neutral plasma chemistry products are usually the easiest to measure. They have, due to their negligible reactivity at the surface, much higher densities in the plasma reactor than short-lived reactive species. They usually have a homogeneous density distribution over the whole reactor volume, so they can be measured outside of the active plasma region or even in the exhaust line. It is important to know densities of these species, because they take part in chemical reactions and they are also dissociated in collisions with electrons. Additionally, time-resolved measurements can reveal information about their origin or about the kinetics of chemical reactions.

The measurements are usually performed with electron energies near the maximum of the EII cross-sections ( $\sim$ 70 eV) and the mass spectra are dominated by CPs and their combinations. The mass spectra are often analysed in a non-quantitative manner by directly interpreting raw signal peaks. However, this method can be misleading since the raw signals refer to ions, which are produced from stable neutrals via direct EII and DEII in the ionizer of the mass spectrometer. Consequently, the signal at a given mass is a linear combination of all (fragment) ions with corresponding m/z ratio. The quantification of the measured signal requires calibration measurements or an estimation of CPs of the species of interest and a mathematical separation of the mass spectra into these CPs.

The most simple mathematical separation of mass spectra is a so-called step-by-step method: first, the CP of a given species known to be in the mixture is determined, either from databases or by direct calibration experiments (the CP is measured at a given density for this single species giving the signal intensity at all peaks of the CP per unit of density). Second, this calibrated CP is re-scaled by a constant factor  $f_s$ and is subtracted from the raw data until the contribution of this single species to the mass spectrum is eliminated. This factor  $f_s$  is proportional to the species density in the case of the directly calibrated CPs or to the product of species concentration or partial pressure and ionization efficiency in the ionizer of the mass spectrometer. This procedure is repeated with the CPs of additional species, which are expected to be in the gas mixture, until all peaks in the mass spectra are accounted for. The factors  $f_s$  are then a measure for the contribution of species s to the gas mixture. The main disadvantage of this procedure is error propagation during consecutive subtractions rendering the factors  $f_s$  very unreliable. A typical consequence are solutions exhibiting negative species densities.

Since the measured mass spectrum is a linear combination of the CPs, the straightforward least-square-method analysis can be used to separate all CPs. A mathematical formulation of the mass spectra problem is defined first. The measured data are expressed as a vector  $\vec{d}$  containing i peaks corresponding to the ions generated via ionization and fragmentation of collected neutrals in the ionizer of the mass spectrometer. The concentrations of stable neutrals in the plasma are expressed as a vector  $\vec{x}$  containing s species. Here, we restrict ourselves to a reasonable set of species, which are believed to be present in the gas mixture. Both vectors are connected by a matrix  $\hat{C}$ containing the CP of each species. The CP matrix  $\hat{C}$  consists of i rows, with each column corresponding to that part of the CP of species s contributing to the mass channels i. A large number of measured mass spectra can be incorporated in a single analysis run. If we use the index j for each new experiment, the mathematical description of the problem can be written as

$$\vec{d}_i = \hat{C}\vec{x}_i \tag{14}$$

and can be solved by the least-square method. This method avoids error propagation, but will still suffer from the possibility of obtaining negative densities. The least-square method is best suited for *over-determined* problems. In many cases, however, some of the CPs are not known or may contain large errors.

These limitation are mitigated using Bayesian statistics, which combines consistently CP, mass spectra and all corresponding errors in a single analysis. Details of this approach are presented by Schwarz-Selinger *et al* [47] and by Kang *et al* [48].

The main goal is the determination of the species with unknown concentrations  $\vec{x}_j$ , which are assumed to be simultaneously present in all experiments  $\vec{d}_j$  given a single CP matrix  $\hat{C}$ , which remains identical irrespective of the experiment.

The solution of the equation (14) is equivalent to the search for the maximum of the likelihood  $p(\vec{d}_j|\vec{x}_j,\hat{C},\vec{S}_j)$  for a given set of data  $\vec{d}_j$ , if the concentrations  $\vec{x}_j$  and the CP matrix  $\hat{C}$  are known. The entries in the data vector  $\vec{d}_j$  may contain an error, which is incorporated in a matrix  $\hat{S}_j$  containing the error  $\epsilon_i$  of mass peak i in experiment j on the main diagonal. The likelihood is given as

$$p(\vec{d}_j|\vec{x}_j, \hat{C}, \vec{S}_j) \propto \exp\left[-\frac{1}{2} \left(\vec{d}_j - \hat{C}\vec{x}_j\right)^{\mathrm{T}} \hat{S}_j^{-2} \left(\vec{d}_j - \hat{C}\vec{x}_j\right)\right]$$
(15)

This likelihood is now inserted into the so-called Bayes theorem [49], to gain an expression for the probability p of the concentrations  $\vec{x}_i$  for a given set of data  $\hat{d}_i$ :

$$p(\vec{x}_j|\vec{d}_j, \hat{C}, \hat{S}_j) = p(\vec{x}_j)p(\vec{d}_j|\vec{x}_j, \hat{C}, \hat{S}_j)/\text{Norm},$$
 (16)

*Norm* refers to a normalization constant, which is irrelevant for the search of the maximum of  $p(\vec{x}_j | \vec{d}_j, \hat{C}, \hat{S}_j)$ . By applying the Bayes theorem, a new probability  $p(\vec{x}_j)$  is introduced, which corresponds to the *prior* for the concentrations  $\vec{x}_j$ . A prior contains *a priori* information regarding the quantity of interest, such as for example the known densities of precursor gases.

In the case of CPs, *prior* information are the calibration experiments or the existence of literature values from CP databases. This prior information is incorporated using the marginalization rule of the Bayes theory: the likelihood is averaged over all possible CPs by weighting this average with the prior information  $p(\hat{C})$ :

$$p(\vec{x}_j|\vec{d}_j, \hat{C}, \hat{S}_j) \propto \int p(\hat{C})p(\vec{d}_j|\vec{x}_j, \hat{C}, \hat{S}_j) dC.$$
 (17)

The main advantage of this formulation of the problem is the fact that the final solution  $p(\vec{x}_j|\vec{d}_j,\hat{C},\hat{S}_j)$  depends on the actual measured data  $\vec{d}_j$ , but also on the CPs  $\hat{C}$ , which might be only known within a certain error margin. The treatment of the CPs and their error margin are therefore of key importance for the final solution. The species concentrations are determined by finding the maximum of the probability

$$p(\vec{x}_j|\vec{d}_j, \hat{C}, \hat{S}_j) \propto \int p(\hat{C})p(\vec{d}_j|\vec{x}_j, \hat{C}, \hat{S}_j) dC.$$
 (18)

The Bayes algorithm produces concentrations as well as *posterior* CPs including corresponding error margins. The *posterior* CPs might differ from *prior* CPs, if the measured data contain enough information to allow for this deviation. If the data are not restrictive for such a deviation of if the *prior* CP are already compatible with the data, the *posterior* and *prior* CPs are almost identical.

Finally, partial pressures are extracted by comparing the calibration measurements yielding the partial pressure  $p_{\text{species}}^{\text{calibration}}$  of a given species, as it is measured during calibration, is direct proportional to the (total) signal intensity  $|\vec{d}^{\text{calibration}}|$  of the measured spectrum. This information is used to determine the partial pressure  $p_{\text{species}}^{\text{plasma}}$  in the actual plasma experiment from the measured data  $|\vec{d}^{\text{plasma}}|$  by

$$p_{\text{species}}^{\text{plasma}}(t) = p_{\text{species}}^{\text{calibration}}(t) \cdot \frac{|\vec{d}^{\text{plasma}}|}{|\vec{d}^{\text{calibration}}|}.$$
 (19)

This approach works only for those species, where a known partial pressure can easily be adjusted in a calibration measurement. If no partial pressure information is available, the partial pressure can be estimated using the total ionization cross-section of measured species and the ratio of total ionization cross-section and partial pressure of some available calibration species. The accuracy of this estimated partial pressure is of course less reliable than the measured partial pressure of directly calibrated species.

The Bayes analysis have been used for the analysis of mass spectra of an  $C_2H_2$  discharge taken with  $100~\mu s$  time resolution in first 4.5~s after plasma ignition, where the high time resolution has been achieved by use of a step-scan procedure [50–53]. All mass spectra have been analysed simultaneously in one analysis with the use of 22~prior CPs. The results are, therefore, very robust with respect to possible errors in single data vectors. In addition, the temporal evolution of the mass spectra resulting from a complex chemistry of many hydrocarbon species after plasma ignition represents a restrictive and informative data set, which allows a quantitative

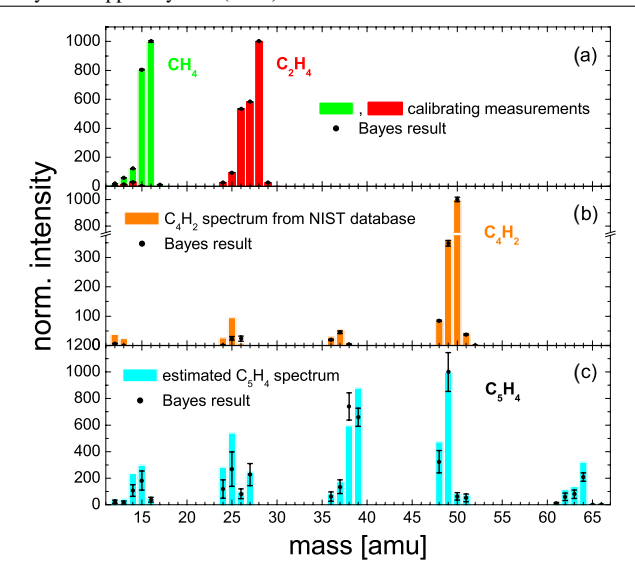


**Figure 12.** *Prior* (bar) and *posterior* (dots with error bars) CPs of species with (*a*) available calibration measurements, (*b*) CP reported in NIST database [54] and (*c*) unavailable and therefore estimated CP. All CPs are scaled to a maximum peak intensity of 1000. For more details see the text. Data taken from [51].

determination of CPs and partial pressures because *all* data are combined in a *single* analysis. In contrast, the quantification of 22 species based on the analysis of only one single mass spectrum is impossible. The *posterior* CPs output data will be discussed here as an example. Figure 12 compares *prior* (bar) with *posterior* (dots with error bars) CPs of calibrated species (a), species with CP taken from NIST database [54] (b), and estimated CP (c). The results are discussed with respect to the different quality of the information that is used to define the *prior* CPs.

The *prior* and *posterior* CPs of directly calibrated  $CH_4$  and  $C_2H_4$  agree very well. The very small error margins indicate the good knowledge of these CPs, because it could be directly measured using  $C_2H_4$  from the gas bottle. The determined partial pressure of this species is very accurate.

The prior CP of C<sub>4</sub>H<sub>2</sub> is taken from the NIST database, because this unstable gas is not easily available for calibration measurements. The CP of C<sub>4</sub>H<sub>2</sub> from NIST can deviate from the CP of C<sub>4</sub>H<sub>2</sub> as it would be directly measured with the mass spectrometer. The larger error margins set on this prior CP give the Bayes algorithm enough flexibility to take the possible discrepancy into account. The corresponding posterior CP shows that the main peaks agree very well with the NIST spectrum. Only differences at mass channels 25 amu and below are visible, corresponding to C<sub>2</sub>H, C<sub>2</sub>, CH and C fragment ions. These fragments are formed from almost any hydrocarbon entering the ionizer, resulting in a massive overlap of CPs, which induces larger posterior errors. The deviation at small masses might also be caused by an uncorrected mass transmission of the spectrometer that was used for the acquisition of the C<sub>4</sub>H<sub>2</sub> NIST spectrum.

The *prior* CP of  $C_5H_4$  is only estimated, based on its known structure and similarity to other hydrocarbon molecules, for which the CPs have been reported. Large error margins are supplied for the Bayes algorithm to take this

uncertainty into account. Large differences between *prior* and *posterior* CP are expected and also observed. The resulting error margins of the *posterior* CPs are a measure for their accuracy: a small error indicates that the measured data contain enough information so that the Bayes analysis yields a unique *posterior* CP and partial pressure; a large error indicates that the measured data are not informative enough. The determined partial pressure of this species is just an upper estimate of its true value. Bayes analysis was also used for the analysis of RF-CCP in CH<sub>4</sub>, where CH<sub>3</sub> and C<sub>2</sub>H<sub>5</sub> radicals were detected in the mass spectrum [55].

It is important to note that the proper choice of error margins is key to the whole Bayes analysis process. Large error margins underestimate the quality of the data and therefore waste information, whereas too small error margins generate large discrepancies between the fit and the experimental data.

Typical examples of neutral species measurements are the measurement of the depletion of precursor gases, the identification and measurement of densities of stable plasma chemistry products or the determination of overall loss or production rates of these species under varying conditions. These data are for example a valuable input for the validation of plasma chemistry models and there exist many reports in the literature. Very illustrative are the works of Doyle *et al* with analysis of CH<sub>4</sub> [56], C<sub>2</sub>H<sub>2</sub> [57] and SiH<sub>4</sub> [58] plasmas, where the MS analysis of gas precursors and stable products is combined with a reaction kinetics model. In particular, the time-resolved measurements in the static discharge (in closed reactor without gas flow) after plasma ignition provided valuable insights into the gas kinetics.

#### 4.2. Measurement of short-lived reactive neutral species

Much more information about the plasma chemistry and surface processes is obtained when the densities of reactive radicals are measured. MBMS, as described previously, has to be used for their detection. Additionally, threshold ionization MS (TIMS) has to be used to avoid dissociative ionization in the ionizer.

The radicals transported with the MB into the ionizer are ionized in the EII process in the same way as stable neutrals. For example, for the detection of  $C_2H$  radicals in a  $C_2H_2$  plasma, the signal at m/z=25, corresponding to  $C_2H^+$  ions, can be measured:

$$C_2H + e^- \rightarrow C_2H^+ + 2e^-$$
 for EE > 11.7 eV.

The ionization threshold of this process is 11.7 eV. The  $C_2H^+$  ions can, however, also be generated in DEII of stable hydrocarbon molecules, in this case  $C_2H_2$ :

$$C_2H_2 + e^- \rightarrow C_2H^+ + H + 2e^-$$
 for EE > 17.1 eV.

The threshold of this reaction is  $17.1 \, \text{eV}$ ,  $5.4 \, \text{eV}$  higher than the threshold for the direct ionization of  $C_2H_2$  into  $C_2H_2^+$  ions, because one C–H bond has to be additionally broken.  $C_2H^+$  ions from DEII of  $C_2H_2$  appear, therefore, in the energy scan at m/z=25 only at electron energies above  $17.1 \, \text{eV}$ .

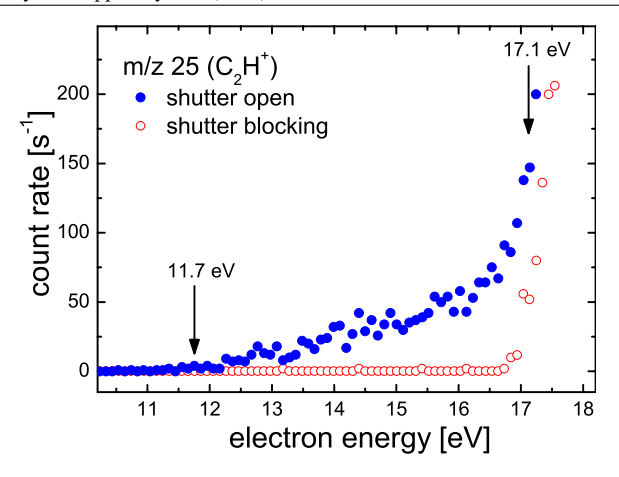


**Figure 13.** Electron energy scan for  $C_2H^+$  ions (m/z = 25) measured with and without the shutter blocking the substrate plane. Reprinted with permission from [59], copyright 2005, Elsevier.

This difference to direct EII of  $C_2H$  enables the detection of the  $C_2H$  radical. The electron energy scan at m/z=25 in  $C_2H_2$  gas with and without plasma in front of the sampling orifice can be seen in figure 13.  $C_2H$  radicals can be measured with an electron energy between 11.7 and 17.1 eV [34, 59]. The disadvantage of TIMS is the fact that the EII cross-section decreases sharply towards the ionization threshold, which results in correspondingly lower sensitivities.

The identification of the species, detected at a given mass, can be achieved by performing an electron energy scan and thereby determining their ionization energy. An example of an identification of hydrocarbon radicals in an expanding thermal argon plasma with  $C_2H_2$  has been given by Benedikt *et al* [34]. The electron energy scan at m/z=38 revealed the presence of reactive  $C_3H_2$  radicals. The measured appearance potential of  $9.2\pm0.2\,\text{eV}$  allowed distinguishing between propargylene (ionization energy  $8.7-8.8\,\text{eV}$ ), cyclopropenylidene ( $9.15\pm0.03\,\text{eV}$ ), and propadienylidene ( $10.43\pm0.02\,\text{eV}$ ) isomers [60]. TIMS can also be used for the detection of metastable particles such as  $N_2$  ( $A^3\Sigma_n^+$ ) [61] or  $O_2(a^1\Delta_g)$  [62].

Many reports of TIMS of radicals can be found in the literature for fluorocarbon [33,63], oxygen [21,64], chlorine [65], silane [66–69] or hydrocarbon [34,35,66–68,70,71] plasmas.

In addition to EII, DEA can also be used at different threshold energies to directly detect stable and reactive species in electronegative gases, as is discussed by Stoffels *et al* [72].

#### 5. Measurement of ion fluxes

Ions impinging on a surface in plasmas are essential for many applications. Their kinetic energy can be manipulated using a bias at the substrates to control surface modification processes such as thin-film deposition, etching or ion implantation [73, 74]. The ion bombardment affects the film structure and the material density, the nucleation rate, the mechanical properties of the layers as well as adhesion [75–79]. Consequently, the energy resolved MS measurement of ion fluxes, namely the IEDF, provides crucial information about many relevant

plasma processes. In the following, we describe the typical energy distribution of the IEDF as well as the species composition of the IEDF in multi component plasma.

#### 5.1. Ion energy distribution functions—energy

The shape of the IEDF is dominated by two effects. (i) frequency - the frequency of the applied bias might be much lower than the ion plasma frequency. Then, the transit time of ions through the sheath is short and the ion energy directly reflects the voltage applied to the substrate. If the frequency is of the order of the ion plasma frequencies or higher, the ions see a modulated potential during their transit through the sheath leading to an averaged energy upon impact. (ii) collisions—charge exchange collisions in the sheath generate new ions which reach the surface at a lower energy compared with the sheath potential. These new ions may also be affected by a modulated sheath potential. Therefore, two classes of IEDFs may be distinguished whether they originate from a low frequency sheath or RF sheaths.

5.1.1. low frequency sheaths—dc or pulsed dc Peter et al [80] used an MS mounted in the grounded cathode to observe the IEDF of H<sup>+</sup> ions arriving at the target for three different power modes; dc, pulsed dc and pulsed ac at low frequency (kHz). While the IEDF in a dc discharge was almost symmetrical with respect to the maximum energy, the IEDFs in pulsed discharges are characterized by a distinct high-energy tail. Since the operating pressure was in the range 1–10 mbar the main features of the measured IEDF could be explained by both charge exchange and elastic processes in the plasma sheath. Radovanov [81] measured Ar<sup>+</sup> and N<sub>2</sub> IEDFs at the substrate position in a low pressure (Townsend) discharge, which can be well described by solving a one-dimensional Boltzmann transport equation with collisions dominated by resonant charge transfer. Furthermore, the shape of the energy distribution appear to be adequately approximated by a shifted Maxwellian. The mean ion energy is proportional to the generated electric field ranging from 3 to 30 eV for given discharge conditions.

An important class of dc or pulsed dc plasmas are magnetron discharges to deposit metallic thin films. Permanent magnets behind the target confine electrons, allowing for an enhanced ionization even at low pressures. This ionization zone has a donut shape given by the  $E \times B$ drift of the secondary electrons ejected from the target. This donut plasma causes a racetrack on the magnetron target due to the intense sputtering. By combining different inner and outer magnets, two configurations are possible: balanced configuration where the strength of the central magnet is equal to the strength of the outer magnets is used for deposition on materials that are thermally sensitive, for example polymer surfaces; unbalanced configuration where the strength of the central magnet is weaker then the strength of the outer magnets achieving open magnetic field lines reaching the substrate suitable for deposition on thermally insensitive materials, for example metals, glass and hard substrates. The investigation of Ar<sup>+</sup> and Ti<sup>+</sup> IEDFs for balanced and unbalanced magnetron

configurations showed three times higher  $Ar^+$  ion fluxes for unbalanced magnetrons compared with balanced magnetrons, while  $Ti^+$  did not change [82]. Furthermore, the average energies of  $Ar^+$  and  $Ti^+$  ions were shifted from  $\sim 1$  eV to values of  $\sim 2$  eV. These values are lower compared with a low density glow discharge due to the thermalization caused by higher plasma densities in magnetron discharges. The deposition rate in unbalanced mode was found to be 10-20% larger than in balanced mode, indicating an enhancement of the titanium density due to elevated sputtering yield presumably due to the higher bias voltage.

The maximum of the ion current above the racetrack was explained by Wendt et al [83] using the electron dynamics. They showed that, regardless of the position at which the secondary electrons originate, they will travel above the centre of the racetrack where the magnetic field is parallel to the cathode surface. Thus, all energetic electrons contribute to ion production above the racetrack. However, electrons emitted at the racetrack position can only reach any other radial positions through their cross field motion, which is limited by the size of the Larmor radius. The result is a concentration of ion production near the racetrack. The measured IEDF of Zn<sup>+</sup> ions at the target centre and the target edge comprise a dominant low-energy peak and a weak high-energy peak, while the Zn<sup>+</sup> IEDF at the racetrack comprise a high-energy tail and a weak low-energy component. The high-energy peak originates from the Thompson distribution of sputtered material ionized by electron impact in the plasma. The Ar<sup>+</sup> IEDF at three positions comprise a low-energy peak, with a high-energy shoulder only at the racetrack region [84].

5.1.2. high frequency sheaths—RF. Radio frequency plasmas (13.56 MHz or higher) can be generated by a capacitively coupling (CCP) or inductively coupling (ICP) of electrical power into the plasma. The sheath potentials are directly affected by the time modulation of the plasma potential. The influence of an RF sheath potential and sheath thickness on the ions diffusing or drifting out of the plasma and being accelerated by the sheath was studied by Kushner using Monte Carlo simulations [85]. It was found that the IEDF is a function of the ion transit time across the sheath. For transit times that are longer compared with the RF period, the IEDF has a single peak attributed to ion experiencing the timeaveraged sheath potential. For transit times shorter than the RF period the ions are accelerated by the sheath potential resulting in IEDF with double peak formation occurring at extremes of the electrode potential. Furthermore, it has been shown that the width of the IEDF depends on the RF frequency [85, 86]. With increasing frequency, the plasma density increases resulting in thinner sheaths. Therefore, the transit time is reduced and ions suffer less from collisions within the sheath.

Wild and Koidl developed a model for the ion transport through a collisional sheath assuming ions to be created in the sheath by symmetric charge exchange [87, 88]. The resulting IEDF exhibits several peaks generated in the RF modulated sheath depending on the start position and start phase. The model was confirmed using a retarding field analyser. A more detailed analysis of the ion transport through the sheath [89] especially at high pressures [90, 91] has been reported recently.

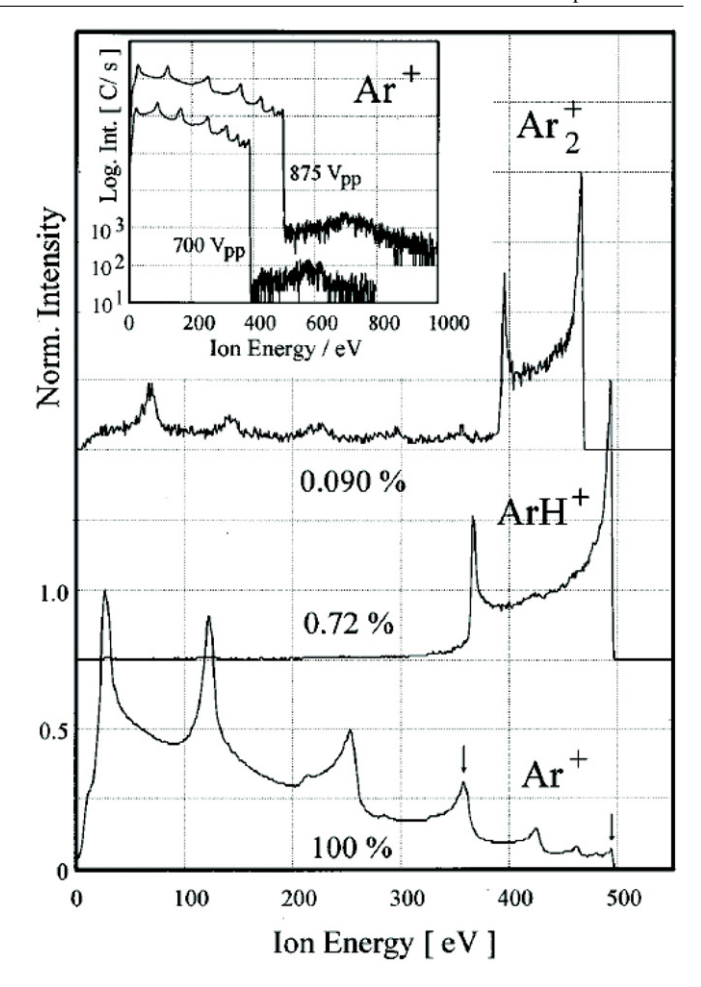


**Figure 14.** Characteristic structures in ion energy distributions in an RF discharge normalized to maximum intensity. Subplot shows generation of Ar<sup>+</sup> from charge transfer of Ar<sup>2+</sup> (reprinted with permission from [92], copyright 1997, American Institute of Physics).

#### 5.2. Ion energy distribution functions—species

Zeuner et al used MS immersed in an RF biased electrode to measure the IEDF of Ar<sup>+</sup> and ArH<sup>+</sup> ions. This is realized by adjusting the MS reference potential to the dc self-bias of the electrode [92]. They have found a double peak IEDF for ArH+ ions and multiple peaks for Ar<sup>+</sup> IEDF. For the given discharge parameters, the probability of creation of ArH<sup>+</sup> in the sheath is very low, therefore a double peak IEDF is consistent with the model of Kushner, figure 14. The discussion of IEDFs, measured directly at the powered electrode, has to be careful. Since it is impossible to float the whole spectrometer with the RF, an oscillating electric field is also created between the aperture, driven by RF or RF and dc bias, and the extractor electrode of the MS that is at a dc self-bias bias. Zeuner et al suggested that this effect could be mitigated by an appropriate distance between the aperture and the extractor electrode, and by a suitable dc potential difference between aperture and extractor [92]. Analogous results were reported by other groups [93–98].

It is known that the discharge parameters influence the properties of the plasma. The influence of pressure and distance on the IEDF of Ar<sup>+</sup> and Cu<sup>+</sup> was investigated by

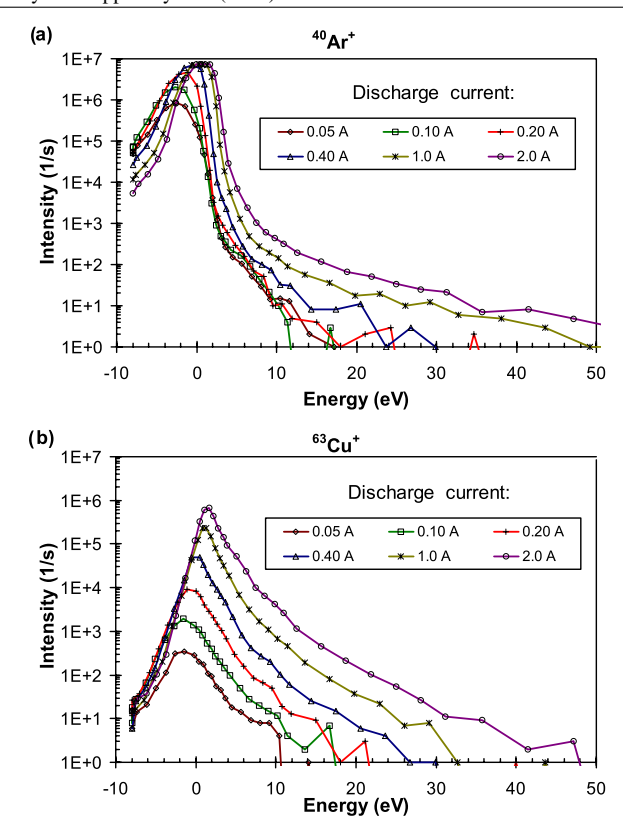


**Figure 15.** Energy distribution of (*a*) Ar<sup>+</sup> and (*b*) Cu<sup>+</sup> ions measured in a dc magnetron sputtering discharge in dependence of the discharge current (reprinted with permission from [99], copyright 2005 Elsevier).

Kadlec *et al* [99]. They found a reduction in the high-energy component and a shift of the main maximum towards low values for both Ar<sup>+</sup> and Cu<sup>+</sup> IEDFs with increasing pressure. The intensity of the low-energy peak of thermalized Cu ions increases with increasing pressure on the expense of the high-energy tail. Similar effects were observed at lower pressures, when the distance between target and the mass spectrometer increased. This can be explained by a loss of energy of sputtered particles in collisions due to an increase in pressure or an increase in distance. They have concluded that the main process influencing the energy distributions is the energy transfer from the sputtered particles to the gas molecules in elastic collisions. Analogous results were reported by other groups [82–103].

Kadlec *et al* [104] studied the influence of the discharge power on the IEDF of Ar<sup>+</sup> and Cu<sup>+</sup> ions. Results show an increase in the intensities for both Ar<sup>+</sup> and Cu<sup>+</sup> IEDF with discharge power, shown in figure 15. The Cu<sup>+</sup> IEDF increase faster compared with the Ar<sup>+</sup> IEDF, especially at low energies. The DSMC simulations showed that for all discharge parameters, the low-energy part is similar to a Maxwellian exponential distribution.

The properties of deposited films can be significantly affected by high-energy particles arriving at a substrate [102, 103, 105]. Takagi *et al* [105] measured the IEDF of the target material and different rare gas species (Ar, Kr, Xe), finding that when the mass number of the target material was larger than that of the rare gas, a high-energy tail in the IEDF was

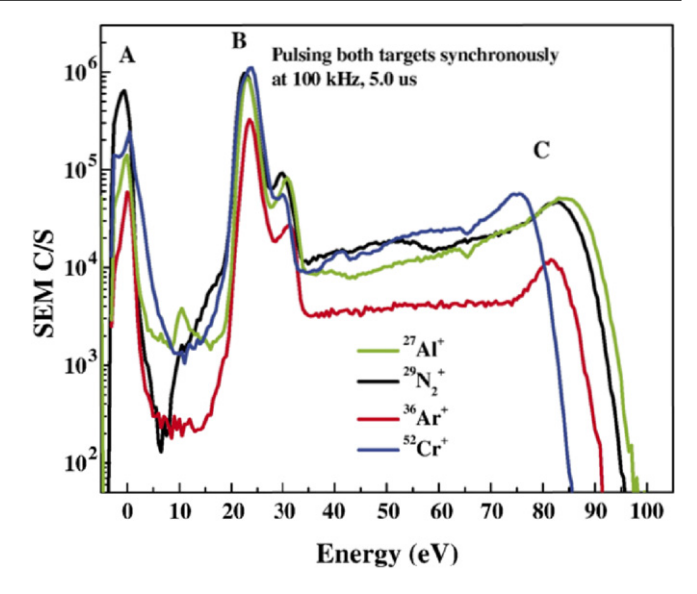


**Figure 16.** The ion energy distributions of various species measured in a pulsed dc magnetron discharge (reprinted with permission from [110], copyright 2007, Elsevier).

observed with energies above  $100 \, \text{eV}$ . The source of high-energy ions is the backscattered gas atoms that are converted to fast ions, by resonant charge exchange in the gas phase. Welzel *et al* [106] reported IEDFs of plasma constituents in reactive dc sputtering of a tungsten target in Ar and  $O_2$  atmosphere. An unusual high-energy tail of  $Ar^+$ ,  $O^+$  and  $O_2^+$  was observed. The authors argued that the origin of the high-energy tail are ions backscattered from the target similar to the explanation of Takagi *et al* [105].

By applying a dc voltage in a pulsed mode, the high-energy tail of the IEDF can be modified. Ar<sup>+</sup> ions with energies up to 10 eV during the on phase were found, in contrast to IEDFs spanning up to 200 eV in the off phase. It was demonstrated that the high-energy ions are created when a high positive plasma potential is generated briefly as a result of grounding the cathode at the end of the on phase [41, 107–112].

A variation of the pulsed dc method is the use of asymmetric bi-polar pulsed dc for sputtering of insulating dielectric materials. It was found that the IEDF of ions in asymmetric bi-polar pulsed dc comprise a low-energy peak, a mid-range peak and a high-energy peak. The shape of the IEDF was explained by showing that the ions emerge from the plasma with a most probable energy corresponding to the plasma potential. Time-resolved measurements showed that the low-energy peak originates in the on phase of the pulse (A), high-energy ions are accelerated by a large positive bias generated by a reverse voltage overshoot phase (C). The midrange ions are created during the off phase (B) when the plasma potential rises a few volts above the positive target potential, figure 16, tagged A, B and C in correlation with the stages of a pulse [113, 114]. The conclusion was that the plasma potential changes occur on the electron plasma frequency time scale [107, 113–116].

One of the methods to additionally increase the ionized fraction of sputtered target material is RF enhanced magnetron sputtering, where the plasma is additionally excited by an RF-driven coil. Measuring the IEDFs in RF enhanced magnetron

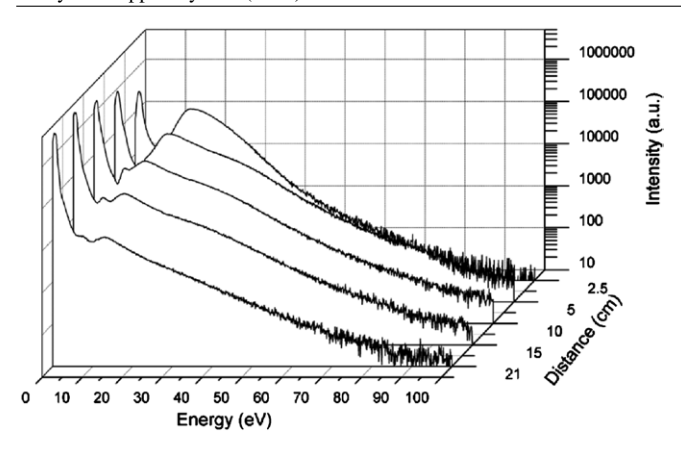


**Figure 17.** The ion energy distribution of Ti<sup>+</sup> ions showing ions with energies up to 100 eV measured in a HIPIMS discharge (reprinted with permission from [126], copyright 2010, American Institute of Physics).

sputtering, the increase in the target material ion fraction reaching the substrate was found. Additionally, the peak energy of the target material IEDF increased by increasing the RF power as a result of elevated plasma potential [117–123].

Another method is high-power impulse magnetron sputtering (HIPIMS/HPPMS) where the power is delivered in short pulses at duty cycles of only a few per cent. The most pronounced features of the IEDF measured in HIPIMS was the existence of higher ionization states such as Ti<sup>4+</sup> ions [124] and a high-energy tail extending up to 100 eV, figure 17 [125, 126]. It has been reported that the time-averaged IEDF can be fitted using the sum of two Maxwellian distributions with different effective ion temperatures originating from the on and off phase of the discharge [127]. Furthermore, the time-resolved measurements show that during the pulse, a Thompson-like high-energy tail distribution of the target material IEDF with energies up to 100 eV has been reported, whereas after the pulse the target material IEDF comprises a main low-energy peak and a high-energy tail [127–129]. Several contributions showed that by increasing the working gas pressure, the highenergy tail of the IEDF was reduced and the low-energy peak of the IEDF increased and narrowed as a result of thermalization [124–135].

An example of an advanced tailoring of the impulse shape is modulated pulse power sputtering technique, resulting in the IEDF being similar to IEDFs created in dc magnetron sputtering with the exception of a higher ionization of the target material [146, 147].

Further ionization of the sputtered material is obtained using the filtered cathodic arc (FCA). The FCA generates highly ionized plasma with average ion energies ranging from 20 to 150 eV, with IEDFs broadening up to several hundred eV [148, 149]. Several groups studying the IEDF reported a reduction in the average energy by increasing the pressure accompanied by a reduction in the average charge state [148–151] due to collisions with the surrounding gas. The IEDFs can be effectively fitted using a single Maxwellian or a combination of two Maxwellians, representing a cold and a hot groups of ions [148].

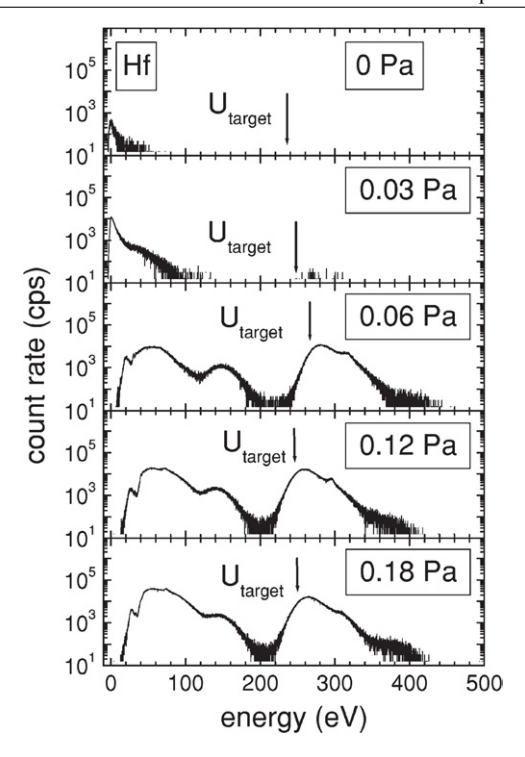


**Figure 18.** Energy distribution functions of O<sup>-</sup> ions in the Hf plasma at five different O<sub>2</sub> partial pressures. The formation of low-medium- and high-energy ions with energies corresponding to half and full of the target potential (indicated by an arrow) is observed (reprinted with permission from [153], copyright 2006, American Institute of Physics).

### 5.3. Negative ions

In many plasmas, negative ions may also be formed either in the bulk due to electron attachment in the case of electronegative source gases or due to electron transfer in surface processes. The detection of these negative ions is challenging, because they are usually confined in the plasma bulk and may not reach the orifice of the MS. In the following, we describe only the example of negative-ion formation in magnetron discharges.

High-energy negative  $O^-$  ions with energies corresponding to the target potential were reported [152]. Several authors confirmed the results with the difference that the most probable energy of the  $O^-$  ions is even larger than the target potential, figure 18 [46, 103, 115, 153]. The IEDF of  $O^-$  comprises three groups of ions, low energy, medium energy and high-energy ions. Mraz *et al* [46, 153], and later Welzel *et al* [103] used theoretical energy distribution of the sputtered material to simulate experimentally measured data. They concluded that the high-energy group consists of the  $O^-$  ions created at the target surface and accelerated in the sheath. The medium energy group is generated by the dissociation of  $O_2^-$  ions followed by an acceleration in the sheath potential. A low-energy group of ions is most probably formed in the extended presheath in front of the magnetron target.

#### 5.4. Time-resolved measurements

The pulsed magnetron technology has been introduced with the aim to improve the deposition of insulating coatings. For any

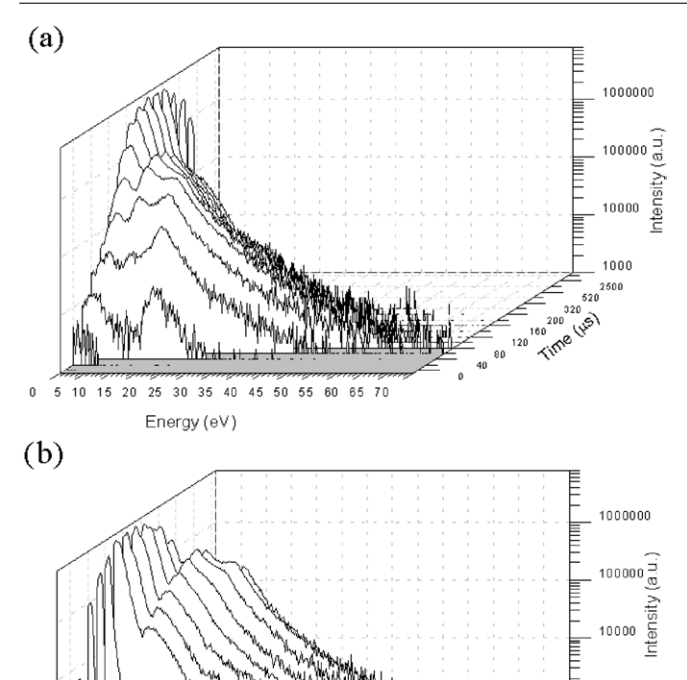


**Figure 19.** Temporal evolution of the ion energy distribution of  $Cr^{\dagger}$  ions with (a) ascending time scale and (b) descending time scale measured in a HIPIMS discharge. Grey area shows on phase of the pulse (reprinted with permission from [128], copyright 2006, IOP Publishing Ltd).

25 30 35 40 45 50 55 60 65 70

understanding of the particle dynamics in the pulsed plasma, time-resolved measurements using energy resolved MS have been performed [114–116, 143, 154, 155].

Some commercial MS instruments have the possibility of gating the signal of the detector and using it in a box car scheme. The temporal resolution is limited to  $10 \,\mu s$ . Time-resolved measurements were performed in a HIPIMS discharge [125, 127-129] where ionization of the sputtered material is up to 80% [156]. Hecimovic et al utilized 20  $\mu$ s acquisition time to observe the temporal evolution of IEDF of Cr<sup>+</sup> ions showing dynamic evolution of the ion energies during and after the pulse, figure 19. Karkari et al introduced a new technique consisting of a modified extractor cap, mounted in front of the orifice, containing two fine meshes insulated from each other and the body of spectrometer. Each mesh could be independently biased synchronously with the discharge pulse to perform the gating function which reduced the resolution to  $2 \mu s$  [114] or even to  $1 \mu s$  [116]. Another method for timeresolved measurements is the use of multichannel scaling cards (MCS). For a fixed mass-to-charge ratio and energy, the signal of the detector is recorded with the MSC with time resolution below  $0.1 \,\mu s$ .

Regardless of the technique, ions arrive at the detector only after a transit time in the MS. In order to reconstruct the exact arrival time of ions at the orifice, the ion time of flight TOF through the MS must be calculated (the equation for the TOF can be provided by the manufacturer). The TOF depends on the ion mass-to-charge ratio and the ion kinetic energy. The dependence on the ion energy can be neglected since for a range of ion energies from 0 to 100 eV the TOF changes only by 5  $\mu$ s, while reported TOF for Ti<sup>1+</sup>, Ar<sup>1+</sup>, Ti<sup>2+</sup>, Ar<sup>2+</sup> is on average 64  $\mu$ s, 58  $\mu$ s, 45  $\mu$ s, 41  $\mu$ s, respectively [125].

## 6. MS of atmospheric pressures plasmas

MBMS can be used to characterize atmospheric pressure plasmas. However, it has to be stressed here, and several examples below provide an evidence for this, that the increased complexity of the gas sampling has to be taken into account. At atmospheric pressure, the Knudsen number Kn at sampling orifice (Kn is a ratio of mean free path, typically 0.1  $\mu$ m at atmospheric pressure, to sampling orifice diameter, 20 to  $100 \,\mu\text{m}$ ) obtains much smaller than one, the gas sampling is collisional and the gas dynamic is determined by continuum flow. The motion of particles is dominated by collisions and thus by diffusion and convection. A pressure gradient towards the sampling orifice exists, which causes the gas molecules to flow through the orifice into the low-pressure region (figure 20). This collisional sampling can negatively influence the plasma and results in the change in the composition of the sampled gas.

#### 6.1. Concise theoretical background

The equation of Hugoniot (1887) can be used to describe the behaviour of continuum flow through the orifice [157]:

$$\frac{dA}{A} + \frac{dv}{v}(1 - M^2) = 0, (20)$$

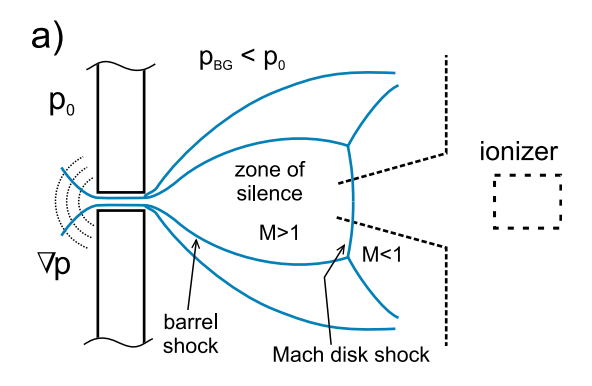
where A denotes the cross-section area, v denotes the flow velocity, and  $M = \frac{v}{c}$  is the Mach number. In the initial stagnation state (i.e. high pressure region), the velocity of the molecules is lower than the speed of sound (v < c, M < 1). So the velocity of the molecules increases with a decreasing cross-section area. If the pressure gradient is sufficiently large, the molecules reach the speed of sound (M = 1) at the minimum cross-section area (dA = 0) called the throat. The cross-section area increases beyond the orifice again, and for M > 1 the flow velocity v further increases reaching supersonic values.

The energy equation [157]:

$$h_1 + h_2 = \frac{1}{2}(v_2^2 - v_1^2) = c_P(T_1 - T_2)$$
 (21)

reveals that the enthalpy h decreases when the flow velocity v increases. In other words, the molecules are accelerated using the heat of the gas. This results in a change in gas temperature described by the right-hand-side of the energy equation. Using the energy equation, one can derive the maximum particle velocity:

$$v_{\text{max}} = c \sqrt{\frac{2}{\gamma - 1} \left[ \left( \frac{P_0}{P_b} \right)^{(\gamma - 1)/\gamma} - 1 \right]}.$$
 (22)



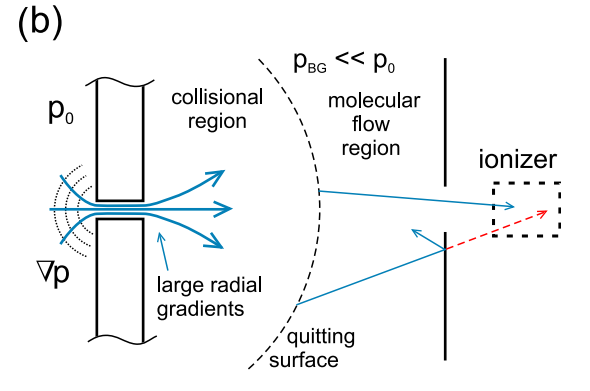


**Figure 20.** Schematic illustration of expansion of a free-jet for two cases: (*a*) expansion into a chamber with significant background pressure and with formation of shock waves and (*b*) expansion into the chamber with negligible background density and continuous transition into the molecular flow regime.

where  $\gamma=c_P/c_V$  is the specific-heat ratio,  $P_0$  and  $P_b$  are the initial stagnation pressure and the background pressure, respectively. By inserting v=c, one obtains the critical pressure ratio  $P_0/P_b$ , which is needed to achieve sonic speed at the throat:

$$\frac{P_0}{P_b} \geqslant G = \left(\frac{\gamma + 1}{2}\right)^{\gamma/(\gamma - 1)}.$$
 (23)

The critical pressure ratio G is less than 2.1 for all gases. If the pressure ratio is lower than the critical ratio G, (super)sonic speed is never obtained and the exit pressure at the orifice is the background pressure  $P_b$ . No further expansion of the gas takes place then. However, if the pressure condition is fulfilled, sonic speed is reached at the throat and the exit pressure is equal to  $P_0/G$ . Since the exit pressure is higher than the background pressure, the gas flow is underexpanded and consequently has to expand into the low-pressure region. The structure of this free-jet expansion [158] is shown in figure 20. This type of expansion is called 'free'-jet because, in contrast to nozzle jets, no diverging nozzle is used to confine the expansion.

The underexpanded gas expands behind the orifice and the pressure in the free-jet decreases with increasing distance to the orifice. A supersonic flow is not able to 'sense' downstream boundary conditions because boundary information cannot propagate with a velocity faster than the speed of sound. Consequently, the free-jet continues to expand even when its pressure falls below the background pressure  $P_{\rm b}$ . Then, the free-jet becomes overexpanded and is recompressed by a

system of shock waves to adjust to the downstream boundary conditions. Shock waves are localized, isentropic zones of large density, pressure, temperature, and velocity gradients. The shock wave at the sides of the free-jet is called 'barrel shock' and at the downstream end 'Mach disk shock' as indicated in figure 20(a). Due to the large density gradients inside a shock wave, they can be characterized by light-scattering methods [159, 160]. The thickness of a shock wave is of the order of the mean free path and the location of the Mach disk  $x_{\rm m}$  (in units of the orifice diameter d) was found to be at

$$\frac{x_{\rm m}}{d} = 0.67 \sqrt{\frac{P_0}{P_{\rm b}}}. (24)$$

The supersonic flow inside these shock waves does not sense any external conditions and is therefore isentropic and independent of the background pressure  $P_b$ . For this reason, the core region is called 'zone of silence'.

For the extraction of a MB, one needs to place a cone-shaped skimmer into the free-jet. However, the exact positioning of the skimmer is crucial. The MB is necessarily extracted from a flow that has not been disturbed by any shock waves. This can be carried out by placing the skimmer upstream of the Mach disk, inside the zone of silence. For example, if the gas expands from atmosphere into a poor vacuum of about 100 Pa background pressure through a sampling orifice with  $100 \,\mu m$  diameter, the Mach disk is located in a distance  $x_{\rm m} \approx 2.1\,{\rm mm}$ . This means that the skimmer must be positioned within the first 2 mm directly behind the sampling orifice, otherwise, the shock waves will significantly distort the MB. Even then, the shape of the skimmer might even be very important to avoid detached shock waves in front of the skimmer. An aerodynamic skimmer design is necessary.

These considerations and challenges can be avoided if no shock waves occur during free-jet expansion. This is the case when the background pressure is such that the mean free path in the first stage is larger than the average length of the system or at least larger than the beam diameter at the position of the second sampling orifice/skimmer. In that case, as an approximation, the free-jet expansion can be divided into two regions, a continuum flow region behind the sampling orifice followed by a free molecular flow [158]. The so-called quitting surface separates both regions. No collisions between the particles in the MB are assumed to take place downstream from the quitting surface. In reality, the quitting surface is not a sharp boundary, but a smooth transition to a collisionless flow. In the case of atmospheric air sampled through an orifice of  $100 \,\mu\mathrm{m}$ diameter, the location of the quitting surface is approximately at  $x_a = 7-10$  mm downstream of the sampling orifice.

The low pressure behind the sampling orifice can be achieved by a combination of a small sampling orifice with a large pumping speed of the vacuum pump, or by pulsing the gas flow through the sampling orifice. Several pulsing schemes have been reported in the past [161–164], where the scheme with the rotating skimmer of Benedikt *et al* [164–167] has been successfully applied for the quantitative characterization of atmospheric pressure microplasmas.

# 6.2. Composition distortion by sampling from atmospheric pressure

An important feature for the absolute density measurements is that the gas composition during the formation of the MB and in the expansion changes. Several effects account for this change and they are known under the name of *composition distortion* [168]. The main contributions to composition distortion are summed up in the following:

Radical recombination at external probe surfaces. The density of radicals diminishes in the vicinity of a surface due to radical recombination [169]. This recombination also takes place at the MBMS sampling orifice and the surrounding surfaces. This effect is negligible if the sampling orifice is at the position of the substrate or when unreactive species are measured.

Acceleration into the sampling orifice. The density determined by MBMS is not the density at the surface without a sampling orifice. The acceleration through the orifice and the drop of the pressure in front of the orifice (see figure 20) cause a distortion of the density profile in front of the surface. The MBMS measures a density at the sampling orifice that is equal to the undistorted density at a certain distance  $\delta$  in front of the wall. This shift of concentration is found to be [168]:

$$\frac{\delta}{d} = 0.19\sqrt{ReSc},\tag{25}$$

where ReSc is the product of Reynolds and Schmidt number and d is the diameter of the sampling orifice. In different experiments the concentration shift was measured and seems to be shifted about 2 up to 5 orifice diameters [168, 170, 171]. Additionally, the pressure gradient and the reduction in the gas density close to the sampling orifice will result in slightly different conditions in the plasma (longer mean free path, higher  $T_{\rm el}$ , higher  $E_{\rm ion}$ ) compared with the situation in front of the substrate. This effect can be reduced by the selection of a smaller sampling orifice.

Chemical relaxation in the free-jet. The chemical relaxation is a shift in the chemical concentration of reactive species due to the falling temperature and pressure in the free-jet expansion. It depends on the ratio between the residence time in the sampling orifice and the relaxation time of the species. If the residence time is smaller than the relaxation time, this contribution to the composition distortion can be neglected. This is the case when an orifice with a maximum length of 0.3 mm is used for sampling from atmospheric pressure [171]. It is worth noting that the sampling orifice does not need to have a very small aspect ratio, because only particles close to the orifice axis, which will not come into contact with the orifice side walls, will stay close to the beam axis and will be detected.

Radial diffusion in the free-jet. Strong radial pressure gradients exist in the free-jet expansion. Hence, pressure diffusion leads to a mass separation downstream from the orifice. It has been shown that heavy species tend to stay on

the central streamline, whereas light species diffuse outwards along the pressure gradients. The enrichment factor  $\alpha_p$  can be estimated by Sherman's formula [168, 172],

$$\alpha_{p} = \frac{n_{H}/n_{L}}{(n_{H}/n_{L})_{0}}$$

$$= 1 + \frac{F(\gamma, x/d)C}{(ReSc)_{0}} \left( \frac{m_{H} - m_{L}}{m_{0}} \frac{\gamma}{\gamma - 1} - \alpha_{0} \right), \quad (26)$$

where n is the number density, ReSc is the product of Reynolds and Schmidt number, C is the viscosity-temperature constant defined by  $(\mu/\mu_0) = C(T/T_0)$ , m is the molecular weight,  $\gamma$  is the specific-heat ratio and  $\alpha_0$  is the thermal diffusion factor. The indices H, L, and 0 refer to heavy species, light species, and stagnation condition, respectively.  $F(\gamma, x/d)$  is a function of the distance and reaches its final value of 13, 16, or 18 for  $\gamma = 5/3$ , 7/5, or 9/7 at a distance of x/d = 3, respectively. The validity of this formula was demonstrated by McCay et al [173] in  $H_2/CO_2$  mixture. The concentration of the heavier  $CO_2$  in the mixture has been enhanced as much as five-fold for their experimental conditions, in very good agreement with calculated enrichment factors.

Skimmer interference. Beam molecules are distorted by collisions with other molecules in the vicinity of the skimmer. Common reasons for distortion are a position of the skimmer orifice close to shock waves, collisions of beam molecules with the inner surface of the skimmer, a blunt skimmer lip, or a too large skimmer orifice. This leads to a decrease in the beam density, an increase in the velocity distribution width, a decrease in the mean velocity, and a distortion of the beam composition. Skimmer interferences can be avoided by a carefully designed skimmer and a low background pressure.

*Mach-number focusing*. Mass separation due to differences in the velocity perpendicular to the beam direction is known as 'Mach-number focusing' or, more precisely, 'speed-ratio focusing'. The perpendicular speed ratio *S* is the quotient of beam velocity divided by the most-probable random speed perpendicular to the beam [157]:

$$S = \frac{v}{\sqrt{2k_{\rm B}T_{\perp}/m}}.$$

Since all gas components in a sampled mixture have nearly the same velocity and temperature after the transition point from continuum to free molecular flow, light species have a lower speed ratio than heavy species. Therefore, light species spread laterally faster than heavy species and are discriminated against heavy ones at the skimmer orifice. (See the blue and red arrow in figure 20(b)).

The distortion of the measured signal due to the latter three effects has been demonstrated by Ellerweg  $et\,al\,$  [166] on He/air mixtures with 1% concentration of neon gas. The ratio of He/air in the mixture has been varied and the neon signal followed. In pure helium, neon atoms are the heaviest species and tend to diffuse slowly in the radial direction compared with light He atoms. However, as air is admixed to the gas mixture, the main collisional partner changes from He to  $N_2/O_2$  molecules and the situation is reversed, the lighter Ne diffuses more quickly in the radial direction and its relative signal

intensity decreases in pure air to only 25% of its original value obtained in pure He. This behaviour is similar for species with similar masses and can be used for the calibration of composition distortion effects [165, 166].

Fragmentation during detection. Since CPs depend on the energy of the parent molecule, the initial temperature of the gas also has an influence on the CPs. One obtains, consequently, different mass spectra for the same gas at different temperatures. However, this effect plays a role only during sampling of high-temperature gases, such as combustion exhaust, and can be neglected for gases near room temperature.

Penetration of the electric field into the sampling orifice. Atmospheric pressure plasmas are characterized by large electron densities and small sheath thicknesses, which are in the range of  $100 \,\mu m$  or below. Due to the high collisionality of the sheaths, very low ion energies are expected consistent with model predictions. However, the detection of these lowenergy ions may be masked by artefacts of the measurement: if the plasma is directly in contact with the sampling orifice, which is for example larger than the sheath width, the sheath will penetrate into the sampling orifice and beyond. The presence of an electric field on the low-pressure side of the sampling orifice will result in an acceleration of the ions to high energies. Ion energies as high as 50 eV, as reported by Rees et al [174] for rf-excited atmospheric plasma in He/air mixture in a so-called plasma needle, may be attributed to this effect. The measurements of the active plasma zone of He/H<sub>2</sub>O plasmas using  $20 \,\mu m$  diameter orifices have shown that only thermalized ions with energies close to the gas temperature are detected [175]. This is an expected result if the sheath is unable to penetrate into the sampling orifice. Ions with tens of eVs of kinetic energy are measured in the same plasma, when a sampling orifice of  $100 \,\mu\mathrm{m}$  was used instead, clearly demonstrating the penetration of the sheath into the lowpressure region in and behind the sampling orifice. A too large sampling orifice has the additional drawback that it generates a larger region with pressure gradient in front of the sampling orifice, which will additionally influence plasma properties and ion energies in this region.

#### 6.3. MS analysis of atmospheric pressure plasmas

The plasma chemistry of cold atmospheric pressure plasmas is rich in many neutral and charged species as demonstrated by recent simulations [176–178]. MS can provide absolute densities and ion fluxes to validate these models and to provide more insight into plasma chemistry processes.

Ion measurement. Many ionic species with complex chemistry are produced in atmospheric pressure non-equilibrium plasmas. Water (whether as impurity or added on purpose) plays a dominant role in many of these discharges in the formation of positive and negative ions. The study of point-to-plain corona discharges (in ambient air or NO<sub>2</sub>, Skalny *et al* [179, 180] and references therein) demonstrates the presence of positive and negative water clusters  $M \cdot (H_2O)_n$  with M = 1

 $O_2^-$ ,  $CO_3^-$ ,  $O_3^-$ ,  $NO^-$ ,  $NO_2^-$ ,  $NO_3^-$ ,  $HCO_3^-$  or  $H_3O^+$ . Some other negative ions, such as  $NO^-HNO_3$  or  $N_2O^-HNO_3$  have been detected as well. Bruggeman *et al* [175] have reported the measurement of positive and negative water ion clusters in the He DBD discharge at different water concentrations. The most important parameters, which determine the relative fluxes of water clusters with given number of water molecules, are (i) the water concentration in the gas mixture and (ii) the travel distance from the plasma, during which the ion-neutral and charge exchange reactions can take place prior to sampling. Additionally,  $He_2^+$  excimer ions or  $O_2^+$  molecular ions have been observed at low water concentrations (330 ppm). An analysis of a helium plasma torch treatment of polymers [181] revealed the presence of  $C_6H_5C_nH_{2n}^+$  ions with n up to 14.

Neutral species measurements. The absolute calibration of neutral particle densities is performed in the similar way to that described in section 4 both for stable or reactive The calibration has to be, however, performed for any gas composition used to account for the possible composition distortion effects [166, 182]. Again, the sampling orifice should be smaller than the sheath width for analysis of the active plasma zone to avoid the plasma generation (and possible reactive particle generation) on the low pressure side of the sampling orifice. Results have been reported for example for the effluent of an He/O2 RF-excited discharge (O and O<sub>3</sub> detection [164-166]) or for the active plasma zone of RF-excited air/He discharge (NO, N and O detection [183, 184]). The MBMS has also been applied to analysis of subatmospheric thermal plasma in Ar/H<sub>2</sub>/CH<sub>4</sub> and Ar/H<sub>2</sub>/SiCl<sub>4</sub> gas mixtures [66].

## 7. Conclusions

Quadrupole mass spectrometry, as a diagnostic technique for the analysis of reactive plasmas at low and atmospheric pressure, has been discussed in this review particle. The basics of its operation principle, the methods of sampling plasma generated species, the calibration methods of neutral species densities or ion fluxes and their energies and many examples from the literature have been given. This review should provide all necessary information for the application of MS for plasma diagnostic and may serve as a starting point for the application of this method or as a motivation to further explore its unique capabilities.

#### Acknowledgments

The financial support of the German Science Foundation (DFG) through the Research Unit 'Physics of Microplasmas' (FOR1123) and Collaborative Research Centre 'Pulsed high power plasmas for the synthesis of nanostructured functional layers' (SFB-TR 87) is gratefully acknowledged.

#### References

- [1] Kogelschatz U 2003 Plasma Chem. Plasma Process. 23 1
- [2] Gross J H 2004 Mass Spectrometry (Berlin: Springer)

- [3] Watson J T and Sparkman O D 2007 Introduction to Mass Spectrometry (New York: Wiley)
- [4] de Hoffmann E and Stroobant V 2007 Mass Spectrometry: Principles and Applications (New York: Wiley)
- [5] Lieberman M A and Lichtenberg A J 2005 Principles of Plasma Discharges and Materials Processing 2nd edn (New York: Wiley)
- [6] Lindsay G and Manga M A 2003 Interactions of Photons and Electrons with Molecules vol Landolt-Börnstein, I/17/C (Berlin: Springer)
- [7] Rejoub R, Lindsay B G and Stebbings R F 2002 Phys. Rev. A 65 042713
- [8] Basner R, Foest R, Schmidt M, Becker K and Deutsch H 1998 Int. J. Mass. Spectrom. 176 245
- [9] Stein S E, 'Mass Spectra' in NIST Chemistry WebBook, NIST Standard Reference Database Number 69 eds P J Lindstrom and W G Mallard (Gaithersburg, MD: National Institute of Standards and Technology) (http://webbook.nist.gov) (retrieved April 29, 2012)
- [10] Stano M, Matejcik S, Skalny J D and Märk T D 2003 J. Phys. B: At. Mol. Opt. Phys. 36 261
- [11] Bartlett P L and Stelbovics A T 2004 At. Data Nucl. Data Tables 86 235
- [12] Tarnovsky V, Levin A, Deutsch H and Becker K 1996 J. Phys. B: At. Mol. Opt. Phys. 29 139
- [13] Baiocchi F, Wetzel R and Freund R 1984 *Phys. Rev. Lett.* 53 771
- [14] Tarnovsky V, Deutsch H and Becker K 1996 J. Chem. Phys. 105 6315
- [15] Ali M, Kim Y, Hwang W, Weinberg N and Rudd M 1997 J. Chem. Phys. 106 9602
- [16] Schram B L, van der Wiel M J, de Heer F J and Moustafa H R 1966 J. Chem. Phys. 44 49
- [17] Hotop H, Ruf M-W, Allan M and Fabrikant I I 2003 Adv. Atom. Mol. Opt. Phys. 49 85
- [18] Christophorou L G 1980 Environ. Health Perspect. 36 3
- [19] Blake R, Monks P and Ellis A 2009 Chem. Rev. 109 861
- [20] Hamers E, van Sark W, Bezemer J, Goedheer W and van der Weg W 1998 Int. J. Mass Spectrom. 173 91
- [21] Agarwal S, Quax G W W, van de Sanden M C M, Maroudas D and Aydil E S 2004 J. Vac. Sci. Technol. A 22 71
- [22] Dylla H F and Blanchard W R 1983 J. Vac. Sci. Technol. A 1 1297
- [23] www.simion.com
- [24] Galejs A and Kuyatt C E 1978 J. Vac. Sci. Technol. 15 865
- [25] Allen J Jr, Durham J, Schweitzer G K and Deeds W 1976 J. Electron. Spectrosc. 8 395
- [26] Craig J J H and Hock J L 1980 J. Vac. Sci. Technol. 17 1360
- [27] Craig J J H and Durrer W G 1989 J. Vac. Sci. Technol. A 7 3337
- [28] Downie P, Reynolds D J and Powis I 1995 Rev. Sci. Instrum. 66 3807
- [29] Liebl H 2007 Applied Charged Particle Optics (Berlin: Springer)
- [30] Perrin J 1997 Plasma Processing of Semiconductors ed P F Williams (Dordrecht: Kluwer) pp 397–432
- [31] Paul W and Steinwedel H 1953 Z. Naturforsch A 8 448
- [32] Blanchard W R, McCarthy P J, Dylla H F, LaMarche P H and Simpkins J E 1986 J. Vac. Sci. Technol. A 4 1715
- [33] Singh H, Coburn J W and Graves D B 1999 J. Vac. Sci. Technol. A 17 2447
- [34] Benedikt J, Agarwal S, Eijkman D J, Vandamme W, Creatore M and van de Sanden M C M 2005 J. Vac. Sci. Technol. A 23 1400
- [35] Benedikt J, Schram D C and van de Sanden M C M 2005 J. Phys. Chem. A 109 10153
- [36] Singh H, Coburn J W and Graves D B 2000 J. Vac. Sci. Technol. A 18 299

- [37] Smith D L, Alimonda A S, Chen C-C, Ready S E and Wacker B 1990 *J. Electrochem. Soc.* **137** 614
- [38] Smith D L and Alimonda A S 1993 *J. Electrochem. Soc.* **140** 1496
- [39] Krähling T, Ellerweg D and Benedikt J 2012 Rev. Sci. Instrum. 83 045114
- [40] Budtz-Jørgensen C, Kringhøj P and Bøttiger J 1999 Surf. Coat. Technol. 116–119 938
- [41] Budtz-Jørgensen C 2001 *PhD Thesis* Faculty of Science, Aarhus University, Denmark
- [42] Perrin J, Lloret A, De Rosny G and Schmitt J 1984 Int. J. Mass Spectrome. 57 249
- [43] Howling A A, Sansonnens L, Dorier J L and Hollenstein C 1993 J. Phys. D: Appl. Phys. 26 1003
- [44] Howling A A, Sansonnens L, Dorier J L and Hollenstein Ch 1994 J. Appl. Phys. 75 1340
- [45] Deschenaux C, Affolter A, Magni D, Hollenstein C and Fayet P 1999 J. Phys. D: Appl. Phys. 32 1876
- [46] Mráz S and Schneider J 2006 Appl. Phys. Lett. 89 051502
- [47] Schwarz-Selinger T, Preuss R, Dose V and von der Linden W 2001 J. Mass Spectrom. 36 866
- [48] Kang H, Preusss R, Schwarz-Selinger T and Dose V 2002 J. Mass Spectrom. 37 748
- [49] Sivia D 1996 *Data Analysis: A Bayesian Tutorial* (Oxford: Oxford University Press)
- [50] Benedikt J, Consoli A, Schulze M and von Keudell A 2007 J. Phys. Chem. A 111 10453
- [51] Consoli A, Benedikt J and von Keudell A 2008 J. Phys. Chem. A 112 11319
- [52] Consoli A, Benedikt J and von Keudell A 2009 Plasma Sources Sci. Technol. 18 034004
- [53] Mao M, Benedikt J, Consoli A and Bogaerts A 2008 J. Phys. D: Appl. Phys. 41 225201
- [54] Nist Atomic Spectra Database 2006 http://www.physics.nist.gov/PhysRefData/ASD/
- [55] Kang H and Dose V 2003 J. Vac. Sci. Technol. A 21 1978
- [56] Dagel D J, Mallouris C M and Doyle J R 1996 J. Appl. Phys. 79 8735
- [57] Doyle J R 1997 J. Appl. Phys. 82 4763
- [58] Doyle J R, Doughty D A and Gallagher A 1990 J. Appl. Phys. 68 4375
- [59] Benedikt J, Eijkman D, Vandamme W, Agarwal S and van de Sanden M 2005 Chem. Phys. Lett. 402 37
- [60] Clauberg H, Minsek D W and Chen P 1992 J. Am. Chem. Soc. 114 99
- [61] Agarwal S, Hoex B, van de Sanden M C M, Maroudas D and Aydil E S 2003 Appl. Phys. Lett. 83 4918
- [62] Benedikt J, Flötgen C and von Keudell A 2010 Society of Vacuum Coaters Technical Conf. Proc. (Orlando, FL) p 393
- [63] Singh H, Coburn J and Graves D 2001 J. Vac. Sci. Technol. A 19 718
- [64] von Keudell A et al 2010 Plasma Process. Polym. 7 327
- [65] Donnelly V M 1996 J. Appl. Phys. 79 9353
- [66] Park S, Liao F, Larson J M, Girshick S L and Zachariah M R 2004 Plasma Chem. Plasma Process. 24 353
- [67] Kae-Nune P 1995 Plasma Sources Sci. Technol. 4 250
- [68] Perrin M, Shiratani J, Kae-Nune P, Videlot H, Jolly J and Guillon J 1998 *J. Vac. Sci. Technol.* A **16** 278
- [69] Kessels W M M, van Assche F J H, Hong J, Schram D C and van de Sanden M C M 2004 J. Vac. Sci. Technol. A 22 96
- [70] Leeds S, May P, Bartlett E, Ashfold M and Rosser K 1999 Diamond Relat. Mater. 8 1377
- [71] Sugai H and Toyoda H 1992 J. Vac. Sci. Technol. A 10 1193
- [72] Stoffels E, Sakiyama Y and Graves D B 2008 IEEE Trans. Plasma Sci. 36 1441
- [73] Anders A 2010 Thin Solid Films 518 4087
- [74] Pelletier J and Anders A 2005 IEEE Trans. Plasma Sci. 33 1944

- [75] Krikorian E and Sneed R J 1979 Astrophys. Space Sci. 65 129
- [76] Mattox D M 1972 J. Vac. Sci. Technol. 9 528
- [77] Håkansson G, Sundgren J, McIntyre D, Greene J and Münz W-D 1987 Thin Solid Films 153 55
- [78] Bunshah R 1994 Handbook of Deposition Technologies for Films and Coatings (Norwich: Noyes Publications)
- [79] Rickerby D S and Matthews A 1991 Advanced Surface Coatings (London: Chapman and Hall)
- [80] Peter S, Pintaske R, Hecht G and Richter F 1993 Surf. Coat. Technol. 59 97
- [81] Radovanov S B, Van Brunt R J, Olthoff J K and Jelenkovic B M 1995 *Phys. Rev.* E **51** 6036
- [82] Hippler R, Wrehde S, Straňák V, Zhigalov O, Steffen H, Tichý M, Quaas M and Wulff H 2005 Contrib. Plasma Phys. 45 348
- [83] Wendt A E, Lieberman M A and Meuth H 1988 J. Vac. Sci. Technol. A 6 1827
- [84] Herrmann D, Oertel M, Menner R and Powalla M 2003 Surf. Coat Technol. 174–175 229
- [85] Kushner M J 1985 J. Appl. Phys. 58 4024
- [86] Makabe T and Petrovic Z 2006 Plasma Electronics: Applications in Microelectronic Device Fabrication (New York: Taylor and Francis)
- [87] Wild C and Koidl P 1989 Appl. Phys. Lett. 54 505
- [88] Wild C and Koidl P 1991 J. Appl. Phys. 69 2909
- [89] Brinkmann R P 2009 J. Phys. D: Appl. Phys. 42 194009
- [90] Brinkmann R P 2011 J. Phys. D: Appl. Phys. 44 042002
- [91] Shihab M, Ziegler D and Brinkmann R P 2012 J. Phys. D: Appl. Phys. 45 185202
- [92] Zeuner M, Neumann H and Meichsner J 1997 J. Appl. Phys. 81 2985
- [93] Hamers E a G, Van Sark W G J H M, Bezemer J, Van Der Weg W F and Goedheer W J 1996 MRS Online Proc. Library vol 420
- [94] Bi Z, Xu X, Liu Y, Jiang X, Lu W and Wang Y 2011 *Plasma Sci. Technol.* 13 181
- [95] Li X, Bi Z, Chang D, Li Z, Wang S, Xu X, Xu Y, Lu W, Zhu A and Wang Y 2008 Appl. Phys. Lett. 93 031504
- [96] Olthoff J K, Van Brunt R J, Radovanov S B and Rees J A 1994 IEE Proc.-Sci. Meas. Technol. 141 105
- [97] Snijkers R J M M, van Sambeek M J M, Kroesen G M W and de Hoog F J 1993 *Appl. Phys. Lett.* **63** 308
- [98] Zeuner M, Neumann H and Meichsner J 1997 Vacuum 48 443
- [99] Kadlec S, Quaeyhaegens C, Knuyt G and Stals L M 1997 Surf. Coat. Tech. 89 177
- [100] Zeuner M, Neumann H, Zalman J, Slavínská D and Biederman H 1998 Vacuum 51 417
- [101] Martin N, Santo A, Sanjinés R and Lévy F 2001 Surf. Coat. Technol. 138 77
- [102] Mišina M, Bradley J, Bäcker H, Aranda-Gonzalvo Y, Karkari S and Forder D 2002 Vacuum 68 171
- [103] Welzel T, Naumov S and Ellmer K 2011 J. Appl. Phys. 109 073302
- [104] Kadlec S, Quaeyhaegens C, Knuyt G and Stals L M 1997 Surf. Coat. Technol. 97 633
- [105] Takagi Y, Sakashita Y, Toyoda H and Sugai H 2006 Vacuum 80 581
- [106] Welzel T, Naumov S and Ellmer K 2011 J. Appl. Phys. 109 073303
- [107] Strauss G and Pulker H 2003 Thin Solid Films 442 66
- [108] Lugscheider E, Bobzin K, Papenfuβ-Janzen N, Maes M and Parkot D 2004 Surf. Coat. Technol. 188–189 164
- [109] Kim Y M, Chung Y M, Jung M J, Vlček J, Musil J and Han J G 2005 Surf. Coat. Technol. 200 835
- [110] Lin J, Moore J, Mishra B, Sproul W and Rees J 2007 Surf. Coat. Technol. 201 4640
- [111] Lin J, Moore J, Mishra B, Pinkas M, Sproul W D and Rees J 2008 Surf. Coat. Technol. 202 1418

- [112] Richter F, Welzel T, Kleinhempel R, Dunger T, Knoth T, Dimer M and Milde F 2009 *Surf. Coat. Technol.* **204** 845
- [113] Bradley J W, Bäcker H, Aranda-Gonzalvo Y, Kelly P J and Arnell R D 2002 Plasma Sources Sci. Technol. 11 165
- [114] Karkari S K, Bäcker H, Forder D and Bradley J W 2002 Meas. Sci. Technol. 13 1431
- [115] Mišina M 2003 Surf. Coat. Tech. 169-170 53
- [116] Voronin S A, Clarke G C B, Čada M, Kelly P J and Bradley J W 2007 *Meas. Sci. Technol.* **18** 1872
- [117] Fukushima K, Kusano E, Kikuchi N, Saito T, Saiki S, Nanto H and Kinbara A 2000 *Vacuum* **59** 586
- [118] Konstantinidis S, Nouvellon C, Dauchot J, Wautelet M and Hecq M 2003 Surf. Coat. Technol. 174–175 100
- [119] Kusano E, Kashiwagi N, Kobayashi T, Nanto H and Kinbara A 1998 Surf. Coat. Tech. 108–109 177
- [120] Kusano E, Kobayashi T, Kashiwagi N, Saitoh T, Saiki S, Nanto H and Kinbara A 1999 Vacuum 53 21
- [121] Kusano E, Saitoh T, Kobayashi T, Fukushima K, Kikuchi N, Nanto H and Kinbara A 1999 Papers from the 45th National Symp. of the American Vacuum Society vol 17, p 2360
- [122] Kusano E, Fukushima K, Saitoh T, Saiki S, Kikuchi N, Nanto H and Kinbara A 1999 Surf. Coat. Technol. 120–121 189
- [123] Molle C, Beauvois A, Wautelet M, Dauchot J and Hecq M 1999 *Vacuum* 53 17
- [124] Andersson J, Ehiasarian A P and Anders A 2008 Appl. Phys. Lett. 93 071504
- [125] Bohlmark J, Lattemann M, Gudmundsson J, Ehiasarian A, Aranda Gonzalvo Y, Brenning N and Helmersson U 2006 Thin Solid Films 515 1522
- [126] Hecimovic A and Ehiasarian A P 2010 J. Appl. Phys. 108 063301
- [127] Hecimovic K, Burcalova A and Ehiasarian A P 2008 J. Phys. D: Appl. Phys. 41 095203
- [128] Hecimovic A and Ehiasarian A P 2009 J. Phys. D: Appl. Phys. 42 135209
- [129] Mishra A, Clarke G, Kelly P and Bradley J W 2009 Plasma Process. Polym. 6 S610
- [130] Aiempanakit M, Helmersson U, Aijaz A, Larsson P, Magnusson R, Jensen J and Kubart T 2011 Surf. Coat. Technol. 205 4828
- [131] Burcalova K, Hecimovic A and Ehiasarian A P 2008 J. Phys. D: Appl. Phys. 41 115306
- [132] Ehiasarian A P, Aranda Gonzalvo Y A and Whitmore T D 2007 Plasma Process. Polym. 4 S309
- [133] Ehiasarian A P, Vetushka A, Hecimovic A and Konstantinidis S 2008 J. Appl. Phys. 104 083305
- [134] Ehiasarian A P, Andersson J and Anders A 2010 J. Phys. D: Appl. Phys. 43 275204
- [135] Greczynski G and Hultman L 2010 Vacuum 84 1159
- [136] Hecimovic A and Ehiasarian A 2011 *IEEE Trans. Plasma* Sci. 39 1154
- [137] Horwat D and Anders A 2010 J. Appl. Phys. 108 123306
- [138] Jouan P, Le Brizoual L, Ganciu M, Cardinaud C, Tricot S and Djouadi M 2010 IEEE Trans. Plasma Sci. 38 3089
- [139] Kudláček P, Vlček J, Burcalová K and Lukáš J 2008 Plasma Sources Sci. Technol 17 025010
- [140] Leroy W P, Mahieu S, Depla D and Ehiasarian A P 2010 J. Vac. Sci. Technol A 28 108
- [141] Lundin D, Larsson P, Wallin E, Lattemann M, Brenning N and Helmersson U 2008 Plasma Sources Sci. Technol. 17 035021
- [142] Poolcharuansin P and Bradley J W 2011 Surf. Coat. Tech. 205 S307
- [143] Vlček J, Pajdarová A D and Musil J 2004 Contrib. Plasma Phys. 44 426
- [144] Vlček J, Kudláček P, Burcalová K and Musil J 2007 Europhys. Lett. 77 45002

- [145] Vlček J, Kudláček P, Burcalová K and Musil J 2007 J. Vac. Sci. Technol. A 25 42
- [146] Lin J, Moore J, Sproul W, Mishra B, Rees J, Wu Z, Chistyakov R and Abraham B 2009 Surf. Coat. Technol. 203 3676
- [147] Lin J, Moore J J, Sproul W D, Lee S L and Wang J 2010 IEEE Trans. Plasma Sci. 38 3071
- [148] Bilek M M M, Martin P J and McKenzie D R 1998 *J. Appl. Phys.* **83** 2965
- [149] Rosén J, Anders A, Mráz S, Atiser A and Schneider J 2006 J. Appl. Phys. 99 123303
- [150] Bilek M M M, Chhowalla M and Milne W I 1997 Appl. Phys. Lett. 71 1777
- [151] Atiser A, Mráz S and Schneider J M 2009 J. Phys. D: Appl. Phys. 42 015202
- [152] Zeuner M, Neumann H, Zalman J and Biederman H 1998 J. Appl. Phys. 83 5083
- [153] Mráz S and Schneider J M 2006 J. Appl. Phys. **100** 023503
- [154] Voronin S A, Alexander M R and Bradley J W 2005 Meas. Sci. Technol. 16 2446
- [155] Voronin S, Alexander M and Bradley J 2006 Surf. Coat. Technol. 201 768
- [156] Hecimovic A 2009 PhD Thesis Sheffield Hallam University
- [157] Pauly H 2000 Atom, Molecule, and Cluster Beams I (Berlin: Springer)
- [158] Scoles G 1988 Atomic and Molecular Beams (Oxford: Oxford University Press)
- [159] Bier K and Schmidt B 1961 The formation of compression-waves in a expanding free gas *Jet. Z. Angew. Phys.* 3 493
  - Bier K and Schmidt B 1961 Z. Angew. Phys. 13 493
- [160] Crist P M S S and Glass D R 1966 AIAA J. 4 68
- [161] Amirav A, Even U and Jortner J 1981 J. Chem. Phys. 75 3151
- [162] Riley J A and Giese C F 1970 J. Chem. Phys 53 146
- [163] Keyser C J, Dembinski M and John P K 1980 Rev. Sci. Instrum. 51 425
- [164] Benedikt J, Ellerweg D and von Keudell A 2009 Rev. Sci. Instrum. 80 055107

- [165] Ellerweg D, Benedikt J, von Keudell A, Knake N and Schulz-von der Gathen V 2010 New J. Phys. 12 013021
- [166] Ellerweg D, von Keudell A and Benedikt J 2012 Plasma Sources Sci. Technol. 21 034019
- [167] Reuter R, Rügner K, Ellerweg D, de los Arcos T, von Keudell A and Benedikt J 2012 Plasma Process. Polym. doi:10.1002/ppap.201100146
- [168] Knuth E 1995 Combust. Flame 103 171
- [169] Smith O I and Chandler D W 1986 Combust. Flame 63 19
- [170] Biordi C P L J C and Papp J F 1974 Combust. Flame 23 73
- [171] Cattolica R J, Yoon S and Knuth E L 1982 Combust. Sci. Technol. 28 225
- [172] Sherman F S 1965 Phys. Fluids 8 773
- [173] McCay T D and Proce L L 1983 Phys. Fluids 26 2115
- [174] Rees J A, Seymour D L, Greenwood C-L, Aranda Gonzalvo Y A and Lundie D T 2010 Plasma Process. Polym. 7 92
- [175] Bruggeman P, Iza F, Lauwers D and Gonzalvo Y A 2010 J. Phys. D: Appl. Phys. 43 012003
- [176] Liu D-X, Rong M-Z, Wang X-H, Iza F, Kong M G and Bruggeman P 2010 *Plasma Process. Polym.* **7** 846
- [177] Hemke T, Wollny A, Gebhardt M, Brinkmann R and Mussenbrock T 2011 J. Phys. D: Appl. Phys. 44 285206
- [178] Graves D 2012 J. Phys. D: Appl. Phys. 45 263001
- [179] Skalny J D, Orszagh J, Mason N J, Rees J A, Aranda-Gonzalvo Y and Whitmore T D 2008 J. Phys. D: Appl. Phys. 41 085202
- [180] Skalny J D, Orszagh J, Mason N J, Rees J A, Aranda-Gonzalvo Y and Whitmore T D 2008 Int. J. Mass Spectrom. 272 12
- [181] Beck A J, Gonzalvo Y A, Pilkington A, Yerokhin A and Matthews A 2009 Plasma Process. Polym. 6 521
- [182] Perrin J 1997 Plasma Processing of Semiconductors (Dordrecht: Kluwer) p 397
- [183] Stoffels E, Aranda-Gonzalvo Y, Whitmore T D, Seymour D L and Rees J A 2006 Plasma Sources Sci. Technol. 15 501
- [184] Stoffels E, Gonzalvo Y A, Whitmore T D, Seymour D L and Rees J A 2007 Plasma Sources Sci. Technol. 16 549